

Modeling carbon accumulation and greenhouse gas emissions of northern peatlands since the Holocene

Bailu Zhao¹, Qianlai Zhuang^{1,2}, Steve Frolking³

¹ Department of Earth, Atmospheric, and Planetary Sciences, Purdue University, West Lafayette, IN 47907, USA

² Department of Agronomy, Purdue University, West Lafayette, IN 47907, USA

³ Institute for the Study of Earth, Oceans, and Space; University of New Hampshire, Durham NH USA

Correspondence to: qzhuang@purdue.edu

Key points:

- Spatially-explicit peat basal age, peat expansion and runoff-runoff are considered for pan-Arctic Holocene simulation
- The pan-Arctic peatlands soil C stock is 396-421 Pg C, and the Holocene average C accumulation rate was 22.9 g C·m⁻² yr⁻¹
- If current permafrost regions thaw, the peat C accumulation rate of the entire pan-Arctic region will decrease

Abstract

Northern peatlands are a large C stock and often act as a C sink, but are susceptible to climate warming. To understand the role of peatlands in the global carbon-climate feedback, it is necessary to accurately quantify their C stock changes and decomposition. In this study, a process-based model, the Peatland Terrestrial Ecosystem Model, is used to simulate pan-Arctic peatland C dynamics from 15ka BP to 1990. To improve the accuracy of the simulation, spatially-explicit water run-on and run-off processes were considered, four different pan-Arctic peatland distribution datasets were used, and a spatially-explicit peat basal date dataset was developed using a neural network approach. The model was calibrated against 2055 peat thickness observations and the parameters were interpolated to the pan-Arctic region. Using the model, we estimate that, in 1990, the pan-Arctic peatlands soil C stock is 396-421 Pg C, and the Holocene average C accumulation rate was 22.9 g C·m⁻² yr⁻¹. Our estimated peat permafrost development history generally agrees with multi-proxy-based paleo-climate datasets and core-derived permafrost areal dynamics. During 500 BP to 1990, the pan-Arctic region went through the Little Ice Age and Anthropocene warming. Under Anthropocene warming, in the freeze-thaw and permafrost-free regions, the peat C accumulation rate decreased, but it increased in permafrost regions. Our study suggests that if current permafrost regions switch to permafrost-free conditions in a warming future, the peat C accumulation rate of the entire pan-Arctic region will decrease, but the sink and source activities of these peatlands are still uncertain.

Plain Language Summary

In this study we used a process-based model, the Peatland Terrestrial Ecosystem Model, to simulate pan-Arctic peatland C dynamics from 15ka BP to 1990. We considered spatially-explicit water run-on and run-off processes, peat basal age and peat expansion process. The simulation shows that in 1990, the pan-Arctic peatlands soil C stock is 396-421 Pg C, and the Holocene average C accumulation rate was 22.9 g C·m⁻² yr⁻¹. During Little Ice Age cooling period and Anthropocene warming, part of pan-Arctic region developed permafrost and thawed, part always had permafrost, and part do not have

permafrost. Under Anthropocene warming, in the freeze-thaw and permafrost-free regions, the peat C accumulation rate decreased, but it increased in permafrost regions. This result suggests if permafrost regions switch to permafrost-free conditions, the peat C accumulation rate of the entire pan-Arctic region will decrease.

1. Introduction

Northern peatlands (north of 30°N) comprise a soil C stock of 415 ± 150 Pg C (Turunen et al., 2002). The Arctic region has been experiencing around three times the global average warming (Allen et al., 2018; Gistemp-Team, 2021) (which might increase regional peatland C release due to the acceleration of peat decomposition (Frolking et al., 2011; Gallego-Sala et al., 2018). In addition to the direct influence of temperature on decomposition, peatlands are also susceptible to indirect influences of climate change and anthropogenic activities. For example, peatland drainage lowers peatland water table and increases decomposition (Huang et al., 2021; Qiu et al., 2021) and peatland fires result in large carbon emissions (Turetsky et al., 2015). Warming-derived permafrost thaw also releases previously frozen soil C, increases dissolved C loss (Gandois et al., 2019), and shifts the microbial community to one that benefits methane emissions (Mccalley et al., 2014).

Peatland C accumulation in permafrost-affected regions under a changing climate is influenced by permafrost dynamics. As permafrost thaws, C in newly thawed soil becomes susceptible to anaerobic and aerobic decomposition (O'donnell et al., 2012; Turetsky et al., 2002). Permafrost thaw can also enhance soil C loss via the outflow of dissolved organic C (Hugelius et al., 2020; Plaza et al., 2019). Several studies have modelled permafrost thaw and subsequent peatland C dynamics under climate warming, indicating that permafrost thaw will cause peats to be a weaker sink of $0.1 \text{ kg C} \cdot \text{m}^{-2}$ or a source of up to $3 \text{ kg C} \cdot \text{m}^{-2}$ during 2015 to 2100 from sporadic and discontinuous permafrost peatlands by 2100 (Jones et al., 2017; Treat, Jones, Alder, et al., 2021). While modeling studies have focused on future permafrost dynamics and their impacts on C balance in the pan-Arctic (Chaudhary et al., 2017; Mcguire et al., 2018), peatland C dynamics impacted by permafrost changes are less studied. Core reconstruction data suggests that pan-Arctic peats went through periods of permafrost aggregation and degradation during the Holocene and that significant permafrost thaw has occurred in the past 300 years (Treat & Jones, 2018). However, less is known on how these peatlands will respond to permafrost dynamics in the region.

Understanding the role of peatlands in future carbon-climate feedbacks is challenging for several reasons, including limited information on peatland distribution and peatland dynamics and a limited number of observational records on peatland initiation time. Modeled peatland spatial extent also has large uncertainties (Qiu et al., 2019; Stocker et al., 2014). In this study, we use a process-based model, the Peatland Terrestrial Ecosystem Model (PTEM), to quantify northern peatland C dynamics by addressing these uncertainties. Current PTEM does not simulate peatland spatial extent dynamics. A previous PTEM simulation study used a fixed peatland area and uniform peat initiation age in the North America, resulting in considerable uncertainties in the estimation of present-day North America peatland C stock (Zhuang et al., 2020). Recently, Chaudhary et al. (2020) generated a spatial map of peatland basal initiation dates for the pan-Arctic region by interpolation from existing datasets of observed basal initiation dates (Gorham et al., 2007; Korhola et al., 2010; Macdonald et al., 2006). However, this method does not give spatially-explicit information on peatland dynamics. Here we address these problems using the following approach: a) for peatland coverage, three northern peatland coverage maps are selected (Hugelius et al., 2020; Melton et al., 2022; Xu et al., 2018), and the soil C stock is estimated

based on different observation-based datasets and the mean of these datasets, respectively; b) a spatially-explicit pan-Arctic peatland expansion trend is established; and (c) we use a machine learning approach to estimate peat initiation year across the pan-Arctic with models trained with observed basal dates.

To examine the impacts of permafrost development history on C cycling, we revised PTEM (Zhao et al., 2022). Compared with the version in Zhuang et al. (2020), the revised PTEM can simulate peat thickness and has an improved soil thermal module (STM) which more accurately simulates the active layer thickness (ALT) dynamics at the site level (Zhao et al., 2022). By comparing peat thickness and ALT, it is possible to simulate peatland permafrost aggregation and degradation through time and analyze the C dynamics corresponding to different permafrost states. This analysis of peatland responses to past climate changes can aid understanding of future peatland C dynamics.

The most recent version of PTEM in Zhao et al. (2022) does not simulate water run-on from the surrounding watershed or lateral water outflow. However, run-on and run-off influence water table depth (WTD) directly (Glaser et al., 2016), transport nutrients in and out of peatlands (Limpens et al., 2006), influence soil pH (Griffiths et al., 2019) which is highly related to CH₄ production (Zhuang et al., 2004), and also influence net N mineralization in both PTEM and experiment (Gao et al., 2016). As peat accumulates vertically, there tends to be a decline in run-on and an increase in run-off, thereby WTD often becomes deeper and fens transition into bogs (Weiss et al., 2006). Meanwhile, with less run-on, the pH of peatlands tends to become lower (Koerselman et al., 1993). With less nutrients brought in by ground water, lower N availability also reduces productivity and decomposition rates (Ojanen et al., 2019; Song et al., 2018). In PTEM, when doing site-level simulations, the transition between fens and bogs and the corresponding decline in productivity and decomposition can be obtained or calibrated from a peat core profile (Zhao et al., 2022). At a regional level, it is also necessary to model the impacts of run-on and run-off dynamics.

Built on the extant PTEM and current understanding of northern peatland thermal, hydrological, and C dynamics, this study: (a) revises PTEM to simulate grid-specific water run-on and run-off; (b) simulates peatland initiation and expansion for each grid cell, and estimates the time-varying peat C stock with different peatland coverage datasets; (c) reconstructs the history of peatland permafrost aggregation and degradation, and (d) analyzes peat C dynamics through the Holocene under different permafrost existence conditions in northern peatlands from initiation to 1990 (Fig. 1).

2. Methods

2.1. Peatland Model Overview

PTEM simulates peatland dynamics at a 0.5°×0.5° resolution. In a previous work (Zhao et al., 2022), PTEM was revised to improve the representation of biogeochemical processes of peatlands. In particular, PTEM models the vegetation C and N pools considering three plant functional types (PFTs): moss, herb and shrub/small trees. Total litter N from the three PFTs is converted into inorganic form by net N mineralization. Net N mineralization influences the amount N available to vegetation, and thereby total productivity of three PFTs. Monthly total litter C from the three PFTs is the monthly litter C input. As litter C from different PFTs will have various decomposition rates, the mean decomposition rate of the monthly peat litter input is the average of three decomposition rates, weighted by the fraction of monthly litter C from each PFT. The peat is divided into 1cm layers from peat bottom to the top, while the top layer can be thinner than 1cm. In each month, new litter C is added to the top layer and peat in all layers decompose. This process usually makes the top layer thicker and the other layers thinner. Thereafter, the layer thicknesses from the bottom to the top are added to get the new peat thickness.

Next, the peat is re-interpolated into 1cm layers and the soil bulk density, soil C content, fraction of remaining original litter and decomposition rate are re-calculated for each layer.

Decomposition in PTEM includes aerobic and anaerobic decomposition. Aerobic decomposition mainly occurs above the water table and is influenced by that layer's temperature and moisture. In PTEM, a monthly soil thermal module (STM) calculates soil temperature in a 25-layer profile with the deepest layer 43.5m below surface (Zhuang et al., 2001). PTEM assumes the top layer is a 10cm moss layer, followed by a soil organic layer. The depth and soil water content of the organic layer in STM is updated monthly, thereby influencing the soil thermal properties. The temperature in each 1cm peat layer is interpolated from the soil thermal profile derived from STM. Soil moisture is calculated by a monthly hydrology module (HM). PTEM divides the soil profile into three hydrological layers: moss, organic and mineral. Water flows vertically from upper to lower layers, and soil moisture in each layer is calculated. Water table depth is calculated by the algorithms in Granberg et al. (1999), which is a function of volumetric moisture in the moss (10cm in this study) and top organic layer (25cm in this study). Above the water table, the effect of soil moisture on aerobic decomposition is modeled to decrease exponentially with the distance between the peat layer and water table. Below the water table, decomposition is dominated by anaerobic processes and the decomposition rate is influenced by temperature and soil pH. Soil pH switches from 6.5 to 4.2 as fens transition to bogs (Zhao et al., 2022). The PTEM fen-bog transition at site-level happens when peat thickness exceeds a certain threshold determined by peat core profiles. As fens shift to bogs, the maximum C assimilation rate of peatlands and litter C decomposition rate of each PFT will decrease by certain fractions, which were calibrated from peat core profiles. At the pan-Arctic level, we assume fen-to-bog transition happens as water run-on declines, leading to lower soil pH (Section 2.2).

2.2 Water run-on and run-off

Water run-off is modelled with the physical equation proposed by Weiss et al. (2006):

$$R_{off} = -\frac{T_r w (dh/dl)}{A} \times m_{day} \times 1000 \quad (1)$$

where R_{off} is run-off ($\text{mm} \cdot \text{mon}^{-1}$), T_r is transmissivity ($\text{m}^2 \cdot \text{d}^{-1}$), w is the vertical width of the hydrological active layer (m) within which WTD fluctuates, dh/dl is the local slope of the water table, A is the unit horizontal area and m_{day} is the number of days within a month. Transmissivity (T_r) is given by:

$$T_r = a_t e^{(-b_t z_{wt})} \quad (2)$$

where a_t ($\text{m}^2 \cdot \text{d}^{-1}$) and b_t (m^{-1}) are parameters given by Granberg et al. (1999), z_{wt} is WTD (m, negative values down from the peat surface).

The GMTED 2010 global 1km resolution DEM data and 1km resolution monthly WTD products Fan et al. (2013) were used to derive the local water table slope. The Fan et al. (2013) dataset was selected because it is based on numerous observations and gives a reasonable estimation of Alaska and Canada wetland areas. Notably, this dataset does not consider any impact of water pumping or drainage on WTD (Fan et al., 2013). For each $0.5^\circ \times 0.5^\circ$ grid, the $1\text{km} \times 1\text{km}$ grids with WTD shallower than 0.25m were picked as wetland grids. In particular, for each of these $1\text{km} \times 1\text{km}$ wetland grids, the local slope of the water table (dh/dl) in eight directions (corresponding to eight neighboring grids) were calculated. Since water table slope is defined as dh/dl along the direction of maximum water head decrease (Cheremisinoff, 1997), the maximum value is picked as the local water table slope. In

169 particular, dl is 1km or $\sqrt{2}$ km depending on the relative location of the two grid cells. dh is the
 170 spatially-explicit difference between WTD in two grids:

$$171 \quad dh = (H_1 + z_{wt1}) - (H_2 + z_{wt2}) \quad (3)$$

172 where H_1 are H_2 are the elevation of two adjacent grids (m), z_{wt1} and z_{wt2} are the WTD of two
 173 adjacent grids (m, negative values suggest below surface), with grid cells indices specified so that dh is
 174 always positive. The local water table slope of all 1km×1km grid cells within a 0.5°×0.5° grid were
 175 averaged to get that grid cell's mean wetland water table slope. Twelve monthly local water table slopes
 176 were calculated for each 0.5°×0.5° grid corresponding to twelve months in the WTD product, and the
 177 annual average was used in the long-term simulation. This grid-specific wetland mean annual water
 178 table slope is assumed as constant throughout the simulation.

179 The algorithm for calculating run-on was adopted and simplified from the Holocene Peatland
 180 Model (HPM) (Frolking et al., 2010), which assumes run-on declines with peat thickness in a sigmoid
 181 function:

$$182 \quad R_{on} = \frac{Ron_{max}}{1 + \exp(a_r \times z_{peat} + b_r)} \quad (4)$$

183 where R_{on} is run-on ($\text{mm} \cdot \text{mon}^{-1}$), Ron_{max} is the maximum run-on of each 0.5°×0.5° grid, a_r (cm^{-1}) and
 184 b_r are fitting parameters and z_{peat} is peat thickness (cm). Ron_{max} was estimated by the maximum run-
 185 off from eight surrounding 0.5°×0.5° grids calculated by Eq. (1), and is a constant for each grid cell. To
 186 estimate a_r and b_r , spatially-explicit trend lines were established describing the decline of run-on with
 187 peat thickness, using the Matlab fitglm function (Appendix Fig. 1). Such a trend line requires at least
 188 three peat thickness and run-on pairs to get an effective estimation. These three points are (1) when peat
 189 thickness is 0cm, run-on is assumed to be Ron_{max} ; (2) under present-day peat thickness, the present-day
 190 run-on is available from calculation; (3) assume when peat thickness is 15m, run-on is 0 $\text{mm} \cdot \text{mon}^{-1}$.
 191 15m-peat thickness is chosen because the thickest peat record in Treat, Jones, et al. (2016b), Hugelius et
 192 al. (2020) and Loisel et al. (2014) is 1460cm. In addition, we also assume run-on declines from Ron_{max}
 193 by 5% when peat thickness is 30cm to improve fitting performance. Therefore, the only unknown pair is
 194 the current peat thickness and current run-on. Before the simulation was run, we did not have our own
 195 estimate of current peat thickness. Therefore, we used an available dataset (Hugelius et al., 2020),
 196 aggregated to 0.5°×0.5° grid to get grid-average peat thickness. In order to estimate current run-on, the
 197 WTD product in Fan et al. (2013) was used as a reference. The 1km resolution WTD in Fan et al. (2013)
 198 was aggregated to 0.5° resolution, and the WTDs of wetland grids (defined as WTD ≤ 0.25m in Fan et
 199 al. (2013)) were averaged as the mean wetland WTD in each 0.5°×0.5° grid. Next, a short-term PTEM
 200 simulation with no run-on or run-off was conducted from 1958 to 2000 to correspond to the period in
 201 Fan et al. (2013), and the spatially-explicit long-term growing season WTD was calculated. If the
 202 spatially-explicit simulated long-term growing season WTD was shallower than the reference growing
 203 season WTD, then the grid should have net run-off and therefore be bog-dominated, otherwise it should
 204 be run-on and fen-dominated. The WTD-related parameters in PTEM were adjusted manually such that
 205 the area fraction of fen-dominated grids agreed with literature (this study: 0.335 vs. Treat, Jones,
 206 Brosius, et al. (2021): 0.339 in Canada and Olefeldt et al. (2021): 0.343 in boreal-Arctic region). PTEM
 207 WTD algorithm is based on Granberg et al. (1999), and the way to calculate total volumetric soil
 208 moisture under the reference WTD is:

$$\begin{cases} Vtot_{ref} = \emptyset \times z_b - z_{wt\ ref\ veg}^2 \times \frac{a_z}{1.5} & z_{wt} \leq z_{\theta\ smin} \\ Vtot_{ref} = \emptyset \times z_b + z_{wt\ ref\ veg} \times \frac{\emptyset - \theta_{smin}}{1.5} & z_{wt} > z_{\theta\ smin} \end{cases} \quad (5)$$

$$a_z = \frac{\emptyset - \theta_{smin}}{z_{\theta\ smin}} \quad (6)$$

where $Vtot_{ref}$ is the total volumetric soil water content (m^3) corresponding to the reference WTD, \emptyset is the total porosity of peat above active layer w , z_b is the lowest WTD (m), θ_{smin} is the lowest volumetric soil moisture at moss surface (the moss layer surface in this study, $m^3 \cdot m^{-3}$), $z_{\theta\ smin}$ is the thickness of the moss layer and a_z is the slope of linear decrease of soil volumetric moisture in the vegetation layer. $z_{wt\ ref\ veg}$ is the reference WTD below the moss surface (m):

$$z_{wt\ ref\ veg} = z_{wt\ ref} - z_{\theta\ smin} \quad (7)$$

where $z_{wt\ ref}$ is the wetland WTD derived from Fan et al. (2013), here used as a reference dataset. The total volumetric soil moisture under the simulated WTD is:

$$Vtot_{sim} = VSM1_{sim} \times z_{\theta\ smin} + VSM2_{sim} \times w \quad (8)$$

where $Vtot_{sim}$ is the total volumetric soil water content (m^3) corresponding to the simulated WTD, $VSM1_{sim}$ is the simulated volumetric soil moisture ($m^3 \cdot m^{-3}$) of the moss layer, $VSM2_{sim}$ is the simulated volumetric soil moisture ($m^3 \cdot m^{-3}$) of the active thickness in the peat layer in PTEM hydrological cycle. The difference between volumetric soil water content (mm) under Fan (2013) wetland WTD and under simulated WTD is:

$$\Delta water = (Vtot_{ref} - Vtot_{sim}) \times 1000 \quad (9)$$

The growing season monthly average run-off ($R_{off\ ref}$, $mm \cdot mon^{-1}$) is still given by Eq. (1), and the growing season monthly average run-on ($mm \cdot mon^{-1}$) is:

$$R_{on\ ref} = \Delta water + R_{off\ ref} \quad (10)$$

This value is used in the current run-on and current peat thickness pair to estimate a_r and b_r in Eq. (4).

The dissolved nitrogen entering the peat is:

$$N_{water} = R_{on\ mon} \times Ncont_{ground} + P_{through\ mon} \times Ncont_{rain} \quad (11)$$

where N_{water} is the monthly nitrogen brought into peat water via run-on and precipitation ($g \cdot mon^{-1}$), $R_{on\ mon}$ is the monthly run-on ($mm \cdot mon^{-1}$), $Ncont_{ground}$ is the nitrogen concentration in ground water ($g \cdot mm^{-1}$), $P_{through\ mon}$ is the monthly precipitation that travels through the canopy and arrives at the ground ($mm \cdot mon^{-1}$), and $Ncont_{rain}$ is the nitrogen concentration in rain water ($g \cdot mm^{-1}$) (Appendix Table 1). In addition, peatland pH is assumed to decrease simultaneously as run-on declines, and the trend is derived from Eq. (4):

$$R_{on} = pH_{min} + \frac{pH_{max} - pH_{min}}{1 + \exp(a_r \times z_{peat} + b_r)} \quad (12)$$

where pH_{min} and pH_{max} are the minimum and maximum pH of peatlands (Appendix Table 1), a_r , z_{peat} and b_r are the same as in Eq. (4).

2.3 Peat initiation

To estimate the basal dates of the grids without available records, a neural network (NN) approach was used (Pedregosa et al., 2011). First, the training data were obtained and processed. Peat basal date data in Loisel et al. (2017), Treat, Jones, et al. (2016c), Treat, Jones, Brosius, et al. (2016) and Yu et al. (2010) were used, selecting only dates with site latitude $\geq 45^\circ\text{N}$ and basal date $\leq 15\text{ka BP}$ ($n = 8590$). These points were grouped into $0.5^\circ \times 0.5^\circ$ grids and the oldest basal date in each grid cell was selected ($n = 1643$) (Fig 2(a)). Independent variables selected to train the NN model included mean annual temperature ($^\circ\text{C}$), precipitation ($\text{mm}\cdot\text{day}^{-1}$), CO_2 concentration (ppm), latitude and longitude, and peat existence (0/1) was the dependent variable. Temperature, precipitation and CO_2 concentration were chosen because they directly influence plant productivity and litter decomposition. Latitude and longitude were chosen because peat plant establishment is related to plant propagule migration from nearby grid cells and is likely to show spatial-autocorrelation (Gorham et al., 2007). The temperature, precipitation and CO_2 concentration data originate from the decadal TraCE 21ka dataset (He, 2011) and were interpolated to $0.5^\circ \times 0.5^\circ$ grids. For each grid cell, a set of input data consisted of five independent variables and one dependent variable was generated for each decade from 15ka BP to 1990. This resulted in 1504 sets of training samples for each grid cell and 2,471,072 sets for all grid cells, which were likely to be sufficient to train the model.

The second step was to train a multi-layer perceptron (NN) model. There were three hidden layers with 16, 64 and 10 nodes in each layer, respectively. In addition, an activation layer was added and the hyperbolic tangent function was selected as the activation function. Eighty percent of these input data were randomly chosen to train the model and the rest were testing samples.

Third, the NN model was applied to the grids without basal records and basal dates were calculated from the NN model outputs. For each grid cell, the model outputs were a time series (10-yr time step) of 0s and 1s, and the peat basal date was defined as the time when outputs switch from 0-dominated to 1-dominated. In order to find this transition, the time series was fitted by Matlab fitglm function and two fitting coefficients were derived for each grid cell (Suppl. Fig, 2). In cases in which the calculated basal dates were older than 15ka BP or younger than 1990 (425/24903 grid cells, 1.7%), an alternative algorithm was used. Assume i is the decade number between 15ka BP and peat initiation, $(1504-i)$ is the decade number between peat initiation and 1990, n_{pos} is the number of 1s in the output time series, $p11$ is the precision score of the model (i.e., the ratio between the true positive number and the total predicted positive number), and $p01$ is one minus $p11$ (i.e., the ratio between the false positive number and the total predicted positive number), then n_{pos} can be calculated as:

$$n_{pos} = i \times p01 + (1504 - i) \times p11$$

$$\text{so } i = \frac{n_{pos} - p11 \times 1504}{p01 - p11} \quad (13)$$

Finally, the basal date (yr BP) corresponding to decade i is:

$$\text{basal} = (1500 - i) \times 10 \quad (14)$$

2.4 Peat expansion

PTEM does not simulate peatland areal shrinkage and expansion within a simulation grid, and spatially-explicit peat expansion in this study originated from downscaling a pan-Arctic peatland

280 expansion trend. At the pan-Arctic scale, the cumulative distribution function (CDF_{reg}) of peat basal age
 281 of $0.5^\circ \times 0.5^\circ$ grids was fitted to a logistic function (Fig. 2(d)):

$$282 \quad CDF_{reg}(\text{basal}) = \frac{1}{1 + \exp[a_c \times (15000 - \text{basal}) + b_c]} \quad (15)$$

283 where a_c and b_c are fitting parameters, and basal is the peat basal date in year BP. This CDF describes
 284 the trend of peat expansion at the regional scale, and we assumed that the same trend is applicable to the
 285 peat expansion in each single grid since initiation (Appendix Fig. 4(a)):

$$286 \quad \begin{cases} f_{peat}(yr) = 0 & yr < \text{basal} \\ f_{peat}(yr) = \frac{1}{1 + \exp[a_c \times (15000 - yr) + b_c]} & yr \geq \text{basal} \end{cases} \quad (16)$$

287 where f_{peat} is the ratio between peat coverage in yr (year) compared with the current peat coverage,
 288 and yr is the simulation year in BP. In the final year of simulation this gives:

$$289 \quad \sum_{j=1}^n f_{peat\ j}(yr) = CDF_{reg}(yr) \times n \quad (17)$$

290 where $f_{peat\ j}(yr)$ is the ratio between peat coverage in yr to the current peat coverage in grid j , and n is
 291 the number of grids included in the simulation.

292 2.5 Pan-Arctic calibration

293 For a regional simulation, calibrating model with a few sites and applying the parameters to the
 294 whole region can cause considerable uncertainties, especially for a 15ka simulation. The estimation of
 295 run-on is also likely to introduce uncertainties due to the dependence on other model-based datasets (i.e.,
 296 Fan et al. (2013); Hugelius et al. (2020) and the hypothetical run-on and peat thickness relationship. To
 297 reduce these uncertainties, we calibrated PTEM with numerous peat thickness records and interpolated
 298 the parameters to the pan-Arctic region using the Kriging method in ArcMAP 10.7. In particular, the
 299 peat thickness records were obtained from Treat, Jones, et al. (2016c), Hugelius et al. (2020) and Loisel
 300 et al. (2014) ($n = 7812$). These records were grouped into $0.5^\circ \times 0.5^\circ$ grids and the thickest peat record in
 301 each grid cell was selected for calibration ($n = 2055$). Peat thickness was chosen for calibration because
 302 it has the most records and can approximately represent the peat soil C. A previous study simulating peat
 303 C accumulation with PTEM at the site level (Zhao et al., 2022) indicates that there are four important
 304 parameters for peat C accumulation: maximum C assimilated by the ecosystem (C_{max}) and heterotrophic
 305 respiration (R_H) at 0°C for the three plant functional types (k_d for moss, herb and shrub/small trees,
 306 respectively). However, with only one peat thickness data value in each grid cell, it's not reasonable to
 307 calibrate four parameters. Therefore, the k_d values were calibrated against the flux tower-based
 308 ecosystem respiration at the Zackenberg, Greenland fen site for 2008-2016 (López-Blanco et al., 2020)
 309 (Appendix Fig. 3) and applied to the whole region, while the C_{max} values were calibrated for the 2055
 310 grids and then spatially interpolated. The calibration was conducted with Model-Independent Parameter
 311 Estimation (PEST, v17.2 for Linux) and the correlation coefficient (r^2) between the observed and
 312 calibrated peat thickness is 0.94 (Fig. 3).

313 2.6. Preliminary model simulations of peat depth-area fraction relationship

314 In PTEM, peat is assumed to be a column of unit area which is vertically divided into 1cm
 315 layers, and the soil C, CO_2 and CH_4 production are calculated for each layer. However, when
 316 considering peat expansion, peat vertical profile is no longer a rectangle, but an irregular shape

described by peat thickness and area relationship (Appendix Fig. 4(d)). Therefore, for a given month, the total soil C, CO₂ and CH₄ production are:

$$SOC_{tot} = \sum_{i=1}^n SOC_i \times f_{peat\ i} \quad (18)$$

$$CO_{2\ tot} = \sum_{i=1}^n CO_{2\ i} \times f_{peat\ i} \quad (19)$$

$$CH_{4\ tot} = \sum_{i=1}^n CH_{4\ i} \times f_{peat\ i} \quad (20)$$

where SOC_{tot} , $CO_{2\ tot}$ and $CH_{4\ tot}$ are the total soil C (g C·m⁻²), CO₂ emission (g C·m⁻² mon⁻¹) and CH₄ production (g C·m⁻² mon⁻¹), SOC_i , $CO_{2\ i}$ and $CH_{4\ i}$ are the soil C, CO₂ emission and CH₄ production in layer i , n is the number of layers and $f_{peat\ i}$ is the ratio between peat coverage in layer i compared with the final peat coverage at the top layer (Appendix Fig. 4(d)). As a result, it is necessary to get the $f_{peat\ i}$ for each layer i . In order to get this information, a preliminary PTEM run was conducted to map the relationships between peat thickness and time, which was used to find the time when peat thickness first exceeds i cm (yr_i) (Appendix Fig. 4(b) & (c)):

$$thick_i = h(yr_i)$$

$$yr_i = h^{-1}(thick_i) \quad (21)$$

where $thick_i$ is integer peat thickness, i is the index of the 1cm peat layer corresponding to $thick_i$. For each given layer i and $thick_i$, $f_{peat\ i}$ was calculated by substituting yr_i into eq. (15) (Appendix Fig. 4(d)). Afterwards, a second PTEM run was conducted with total soil C, CO₂ emission and CH₄ production calculated as eq. (18-20).

2.7 Model input data and simulation analysis

PTEM requires monthly temperature (°C), precipitation (mm·mon⁻¹), cloudiness (0-1) and vapor pressure (hPa) as climate inputs. For the short-term WTD simulation, the climate data was derived from CRU v4.03. For the Holocene simulation, the climate inputs were derived from monthly TraCE 21ka dataset (He, 2011). In particular, vapor pressure data were calculated from TraCE 21ka relative humidity and temperature, and all four climate inputs were bias-corrected by CRU v4.03 data (Zhao et al., 2022). In addition, PTEM requires atmospheric [CO₂] as an input, which was derived from the TraCE 21ka dataset. The other inputs include spatially-explicit soil texture (Fao/Unesco, 1974) and elevation (Zhuang et al., 2002).

Uncertainties in the peatland C stock partially arise from uncertainties in peatland coverage. Since PTEM does not simulate peatland coverage, we use three different maps covering the pan-Arctic region (Hugelius et al., 2020; Melton et al., 2022; Xu et al., 2018). All maps were aggregated into 0.5°×0.5° grids with spatially-explicit peatland abundance, and their average was used as a fourth map. The simulated results were mapped over different peatland extents to get a range of regional soil C and soil C decomposition.

3. Results

3.1 Estimates of regional peat basal dates

We use 24901 grids in the region for model simulation, 23478 of them have predicted basal dates. In Eurasia, with insufficient training data, the predicted basal dates show unrealistic latitudinal patterns (Fig. 2(b)). However, most of these patterns are located in the region with low peatland

coverage, and so should have limited influence on our regional simulation results (Fig. 2(c)). When applying the model to the testing datasets, the accuracy of the neural network model is 0.88, and F_1 score is 0.89, precision score and recall score are 0.87 and 0.90, respectively, indicating the model predicted peat existence with relatively high accuracy. When applying the model with training datasets, the model accuracy, precision score and recall score are the same as applying to the testing datasets. Therefore, no over-fitting was detected in the model. The correlation coefficient (r^2) between the cumulative distribution function (CDF) of the training and predicted datasets is 0.99 (Fig. 2(d)). The CDF suggests that most of the peat initiated during 11ka BP-4 ka BP.

3.2 Regional soil C stocks and C fluxes

The simulated C accumulation rate (CAR) is first compared with other estimates from literature (Loisel et al., 2014; Nichols & Peteet, 2019). The CAR is $22.9 \text{ g C}\cdot\text{m}^{-2} \text{ yr}^{-1}$ during 15 ka BP-1990. The 500-yr bin CAR generally declined from 10ka BP ($30.0 \text{ g C}\cdot\text{m}^{-2} \text{ yr}^{-1}$) to present ($16.8 \text{ g C}\cdot\text{m}^{-2} \text{ yr}^{-1}$) (Fig. 4(a)). This trend agrees with the core-derived data in Loisel et al. (2014) until 1.5 ka BP, when the cores suggest increasing CAR during 1.5 ka BP to present (Fig. 4(a)). The correlation coefficient (r^2) of long-term core-derived CAR and the simulation-derived CAR is 0.25 (Fig. 4(b)). In addition, our simulated trend agrees with the trend in Nichols and Peteet (2019) (minimum soil C scenario), although our estimates are higher after 5 ka BP (Fig. 4(a)).

The contemporary (c. 1990) peatland C stock is 396-421 Pg C depending on the peatland coverage maps, with 404 Pg C corresponding to the average coverage (Table 1). Although peat C started accumulation since 15ka BP, no significant increase is found until 11-12 ka BP (Fig. 5(a)), when peat C accumulation, CO_2 and CH_4 emissions increase simultaneously. In 1950 (0ka BP), with average peatland coverage, the smoothed annual total decomposition is $303.9 \text{ Tg C}\cdot\text{yr}^{-1}$ (Fig. 5(b)).

3.3 Regional permafrost states in peatlands

In order to evaluate the accuracy of PTEM in simulating ALD and permafrost in peatlands, the model results are compared with multiple datasets (Brown et al., 2000; Calm, 1991-; Hugelius et al., 2020; Obu et al., 2020; Treat, Jones, et al., 2016c; Yi & Kimball, 2020). In particular, the simulated ALD in 1990 correlates better with satellite-derived Arctic ALD in 1997 (Obu et al., 2020) and satellite-derived Alaskan ALD in 2001 (Yi & Kimball, 2020) ($r^2=0.66$ and 0.33 , respectively) than with the circumpolar observation network data from (Brown et al., 2000; Calm, 1991-) ($r^2=0.14$, Fig. 6(a-c)). When comparing the simulated permafrost existence in peat in 1990 with the core record (Hugelius et al., 2020; Treat, Jones, et al., 2016c), the accuracy is 0.75 ($n=1504$, Fig. 6(d)). Overall, PTEM captures permafrost existence/absence in peat, especially in continuous permafrost and non-permafrost regions.

In the permafrost region, the deepening ALD from 15ka BP to 7ka BP indicates the part of permafrost became warmer during this period (Appendix Fig. 6). However, this warming trend was mild and did not cause permafrost distribution area shrink (Appendix Fig. 5 & 7). With the accumulation of peat, permafrost area started to expand after 9ka BP, and continued to 7ka BP (Fig. 6). After 7ka BP, an increasing trend in permafrost area was simulated for part of the pan-Arctic region, which peaked during 500a BP- 250a BP (Appendix Fig.7). The permafrost area increasing during 7ka BP-1ka BP was mild compared with the trend after 1ka BP (Appendix Fig. 5). Although ALD in the cooling permafrost region became shallower, the cooling was not severe enough to expand permafrost into most of the originally non-permafrost region except for the European southern permafrost boundary during 3ka BP-1ka BP (Appendix Fig. 7). Under both cooling permafrost and peat accumulation, permafrost expansion in peat was faster during this period and peaked during 3ka BP-1ka BP (0.86 Mkm^2 under average

peatland coverage, Fig. 6, Fig 8). Notably, while the northern permafrost became colder during 7ka BP-1ka BP, the southern permafrost mostly became warmer (Appendix Fig. 6). During 1ka BP-750a BP and 750a BP-500a BP, ALD showed more dynamics than before 1ka BP. In particular, during 1ka BP-750a BP, permafrost area increase continued for northern and southern permafrost regions while permafrost degradation dominated the middle permafrost region; during 750a BP-500a BP, ALD in most permafrost regions became deeper except for the northern permafrost regions in Eurasia (Appendix Fig. 6). During 1ka BP-500a BP, occasional soil and peat permafrost expansion and shrinking was simulated at the southern permafrost boundary (Appendix Fig. 7, Fig. 7).

More severe changes in ALD and permafrost existence were found after 500a BP. During 500a BP-250a BP, a significant permafrost aggradation trend covered most of the permafrost regions (Appendix Fig. 5 & 6), with permafrost distribution expanded at the southern permafrost boundary (Appendix Fig. 7, Fig. 6). After 250a BP, a severe and overwhelming permafrost degradation trend covered the pan-Arctic region, with more deepening ALD in the southern permafrost (Appendix Fig. 5 & 6). At the southern permafrost boundary, the region that developed permafrost in peat during the cooling in 500a BP-250a BP mostly thawed, together with some regions that developed permafrost before 250a BP (Fig. 7).

3.4 Changes in C fluxes during 500a BP-1990

The study region was categorized into three types of grids: ones that developed permafrost during 500a BP-250a BP and thawed by 1990 ('freeze-thaw'), permafrost grids and permafrost-free grids. Fifty-year means of three time slices were used, including 500a BP-450a BP, 275a BP-225a BP and 1940-1990 to compare their C dynamics under different climate and permafrost conditions (Fig. 9). The temperature variation during these three periods is similar under all permafrost conditions. In particular, for the freeze-thaw, permafrost and permafrost-free grids, the median temperature in 500a BP-450a BP dropped by 1.1°C, 0.5°C and 0.7°C in 275a BP-225a BP, respectively, then increased by 0.9°C, 1.5°C and 1.0°C in 1940-1990, respectively (Fig. 9 1(a-c)). Therefore, the permafrost region showed the least cooling and the most warming. Meanwhile, from 500a BP-450a BP to 275a BP-225a BP, the median permafrost-free peat thickness in the freeze-thaw and permafrost regions are similar (differ by 1.1cm and 1.9cm, respectively). In contrast, this value in the permafrost-free region is larger (4.0cm). From 275a BP-225a BP to 1940-1990, under warmer climate, the median permafrost-free peat thickness in the freeze-thaw, permafrost and permafrost-free regions all increased by 10.0cm, 10.6cm and 6.9cm, respectively (Fig. 9 2(a-c)). Notably, the permafrost-free peat thickness is the minimum of ALD and peat thickness. In the permafrost-free and freeze-thaw region, this value is often peat thickness, while in the permafrost region, this value tends to be ALD (Appendix Fig. 8). Median decomposition in the freeze-thaw, permafrost and permafrost-free regions show the same trend that 275a BP-225a BP was the lowest (126.5, 75.6 and 140.1 g C · m⁻² yr⁻¹, respectively), following by 500a BP-450a BP (137.7, 75.8 and 143.1 g C · m⁻² yr⁻¹) and 1940-1990 (156.1, 85.7 and 158.2 g C · m⁻² yr⁻¹) (Fig. 9 3(a-c)). Notably, the decomposition rate in warmer permafrost-free regions were generally higher than that in the colder freeze-thaw regions and the coldest permafrost regions. During 500a BP-450a BP, the median decomposition in the freeze-thaw and permafrost-free regions differed by 5.4 g C · m⁻² yr⁻¹, while this difference enlarged to 13.6 g C · m⁻² yr⁻¹ as permafrost aggregated in the freeze-thaw region. Therefore, for the freeze-thaw region, the lower decomposition in 275a BP-225a BP was not only caused by lower temperature, but also permafrost aggregation.

For the freeze-thaw and the permafrost-free regions, median NPP mainly kept increasing from 500a BP to 250BP and from 250BP to 1990 (by 8.4, 4.6 and -0.1 g C · m⁻² yr⁻¹). However, for the

permafrost region, median NPP first slightly declined then increased (89.8 to 88.5 to 101.3 g C·m⁻² yr⁻¹) (Fig. 9 4(a-c)). For the freeze-thaw and the permafrost-free regions, as a result of lower decomposition, the CAR in 275a BP-225a BP was the highest (30.2 and 20.2 g C·m⁻² yr⁻¹), higher than that in 500a BP-450a BP (10.1 and 10.6 g C·m⁻² yr⁻¹) and in 1940-1990 (19.9 and 9.1 g C·m⁻² yr⁻¹). Notably, as a result of the lower decomposition in the freeze-thaw region, the median CAR was 10.0 g C·m⁻² yr⁻¹ higher than the permafrost-free region during 275a BP-225a BP. For the permafrost region, the CAR kept increasing from 500a BP-1990 (12.8 to 13.0 to 15.6 g C·m⁻² yr⁻¹) (Fig. 9 5(a-c)).

4. Discussion

4.1 Peatland C stocks and fluxes

Our estimated northern peatland soil C stock is 396-421 Pg C depending on the peatland coverage (Table 1). This range agrees with the values in Qiu et al. (2019), Hugelius et al. (2020) and Spahni et al. (2013), is lower than the values reported by Nichols and Peteet (2019), Yu et al. (2010), Loisel et al. (2014), Gorham (1991), and higher than the values in Hugelius et al. (2013) and Müller and Joos (2021). The soil C spatial correlation (*r* value) between this study and Qiu et al. (2019) is 0.38-0.47 depending on peatland coverage map, is 0.49-0.60 between this study and Hugelius et al. (2013), and is 0.69-0.88 between this study and Hugelius et al. (2020) (Appendix Table 2). There are two reasons that the correlation with Hugelius et al. (2020) is higher than that with the other two datasets. First, the run-on parameters were calculated based on the peat thickness data in Hugelius et al. (2020), and run-on influences WTD and thereby decomposition in PTEM (Zhao et al., 2022). Second, the soil C in Hugelius et al. (2020) was derived by machine learning approach and the training samples include data from thousands of peat cores. In this study, spatially-explicit peat C is sensitive to the C_{max} value derived from regional calibration, and the dataset used in our regional calibration has a substantial overlap with the training samples in Hugelius et al. (2020). In general, both the spatial pattern and regional total of peat C in this study agrees with multiple previous studies.

The spatially-explicit CAR from peat initiation 1990CE is presented in Appendix Fig. 9. An obvious discrepancy between our simulated pan-Arctic temporal CAR trend and the core-derived CAR trend in Loisel et al. (2014) is that the simulated 500-yr bin CAR was lower during 1.5ka BP-present (Fig. 4(a)). However, this discrepancy with Loisel et al. (2014) is also found in Nichols and Peteet (2019) and Chaudhary et al. (2020), both of which are modeling studies covering all northern peatlands. A reason for this discrepancy could be that the core-derived CAR for shallow peat samples can be biased high, due to incomplete decomposition of shallow peat (Young et al., 2019). Furthermore, the core-derived long-term CAR generally agrees with the simulated CAR in the corresponding 0.5°×0.5° grids, indicating the discrepancy in CAR in the recent millennia could be a result of insufficient core sample availability. However, the regional long-term CAR values were the same in this study and Loisel et al. (2014) (22.9 g C·m⁻² yr⁻¹ vs. 22.9±2 g C·m⁻² yr⁻¹, Table 1). This CAR value is higher than the core-derived value in Yu et al. (2009) and model simulation in Chaudhary et al. (2020) by 4.3 g C·m⁻² yr⁻¹ and 1.5 g C·m⁻² yr⁻¹, respectively, but falls within the range of Nichols and Peteet (2019), Turunen et al. (2002) and Treat, Jones, et al. (2016a).

4.2 Holocene permafrost aggregation and degradation

The simulated ALD in 1990 correlates most closely with a satellite-derived ALD in 1997 (Obu et al., 2020), followed by a satellite-derived ALD in 2001 (Yi & Kimball, 2020) and observed ALD in different years (1990-2021) ((Brown et al., 2000; Calm, 1991-) (Fig. 6). The better correlation is found when the temporal gap between two datasets is smaller and when more grids are available for

comparison, while the difference in remote sensing estimation methodology may also influence the correlation. As ALD becomes deeper across the northern hemisphere (Luo et al., 2016), the difference between ALD in 1990 and 1997 should be less than the difference between 1990 and 2001, and between 1990 and various years during 1990-2021. Similarly, most of the bias between simulated permafrost-in-peat in 1990 and core observation occurs in the southern permafrost region while the cores data show no permafrost (Fig. 6(d)). Previous study has suggested severe ALD deepening and permafrost degradation in the southern permafrost region during 1982-2015 (Peng et al., 2020). As the cores were mostly collected after 1990 (Hugelius et al., 2020; Treat, Jones, et al., 2016a), it is possible that some cores in this region having deep ALD in 1990 were thawed by the time of core collection.

Consistent with the paleo-temperature database, TraCE dataset shows that Holocene global mean surface temperature reached peak around 6.5 ka BP during the Holocene Thermal Maximum (HTM) (Kaufman et al., 2020) (Appendix Fig. 10), the simulated ALD generally became deeper until 7ka BP. During 7ka BP-6ka BP, a multiproxy paleo-climate dataset indicates that Neoglacial cooling started in the northern hemisphere, with different start time in different regions (Mckay et al., 2018). This cooling trend is consistent with the decrease of ALD during 7ka BP-5ka BP simulated in this study (Appendix Fig. 6). Meanwhile, the peat core data indicate permafrost development in Alaska, Siberia and Arctic Canada before 4ka BP (Treat & Jones, 2018), which is consistent with the permafrost in peat distribution in 7ka BP and 5ka BP (Fig. 7). During Neoglacial cooling, we simulated a widespread permafrost expansion which peaked during 3ka BP-1ka BP. Both our simulation and core data suggest permafrost distribution increased in Arctic Canada, eastern Northern America, and Arctic and European Russia after 3ka BP (Treat & Jones, 2018). After 1ka BP, the simulation showed deepening ALD in most of the permafrost regions during 1ka BP-500a BP, which was approximately Medieval Climate Anomaly (MCA) when most of Eurasia Arctic and parts of North America warmed (Mann Michael et al., 2009). During 500a BP-250a BP, ALD generally became shallower in permafrost region (Appendix Fig. 6), with permafrost expansion found in west Eurasia. This period is approximately the Little Ice Age (LIA), when cooling dominated the Northern Hemisphere (Mann Michael et al., 2009). The deepening of ALD and permafrost coverage shrink in west Eurasia after 250a BP reflects the increase of greenhouse gas emissions, radiative forcing and temperature since 1750 (Ipcc, 2007). In general, the temporal trend of the simulated ALD and permafrost in peat agrees with the paleo-climate dataset and core information.

4.3 Influence of climate change on peat carbon accumulation rate

During 500a BP-250a BP, the onset of the LIA triggered permafrost aggradation in west Eurasia, which made the median CAR $10.0 \text{ g C} \cdot \text{m}^{-2} \text{ yr}^{-1}$ higher than that in the permafrost-free region. From the LIA to the Anthropocene warming, the freeze-thaw and the permafrost-free region had the highest CAR during LIA. This is consistent with the core-based study in the discontinuous and sporadic permafrost region, indicating CAR was the highest during LIA (Zhang et al., 2018). However, for the permafrost region, CAR was the highest during 1940-1990 and the same trend is found in western Canada that rapid surficial C accumulation makes up for the deep soil C loss (Heffernan et al., 2020). Under Anthropocene warming, with a similar increase in NPP in three regions ($8.5\text{-}13.2 \text{ g C} \cdot \text{m}^{-2} \text{ yr}^{-1}$), the different responses of CAR result from the different increases in decomposition rates. Previous studies suggest that both CH_4 and CO_2 emissions increase approximately exponentially with temperature below 25°C (Curiel Yuste et al., 2007; Lupascu et al., 2012). Therefore, under the relatively cold climate in the pan-Arctic, the similar temperature increase has different effects in the warmer southern region and colder northern regions. In particular, in the warmer freeze-thaw and permafrost-free region, median decomposition rates increased by $18.1\text{-}29.6 \text{ g C} \cdot \text{m}^{-2} \text{ yr}^{-1}$, but $10.1 \text{ g C} \cdot \text{m}^{-2} \text{ yr}^{-1}$ in the colder permafrost region, lower

than the median NPP increase. Therefore, Anthropocene warming enhances C accumulation in the permafrost peat, but weakens the C sink in the newly thawed and permafrost-free peat.

Our study agrees with previous modelling, indicating that northern peatlands are still a C sink, and regional NPP has increased more than decomposition under Anthropocene warming (Qiu et al., 2019). Furthermore, peatlands will still be a C sink until at least 2100 under various RCP conditions (Mcguire et al., 2018; Qiu et al., 2020). These modeling studies indicate that despite decomposition increasing more rapidly than NPP under warming conditions, the warming during 1750-2100 does not make decomposition high enough to override NPP. However, temperature is very likely to keep increasing after 2100 (Palmer et al., 2018), resulting in further permafrost warming (Peng et al., 2020) and permafrost degradation in various regions (Czerniawska & Chlachula, 2020; Plaza et al., 2019). As a result, part of the current permafrost region will likely switch to newly-thawed or permafrost-free conditions, where decomposition increases faster than NPP does under the same warming. For instance, by 2100, the northern peatland C sink is projected to be stronger under RCP 2.6 and 6.0 while weaker under RCP 8.5 (Qiu et al., 2020). When projected to 2300, under severe warming scenarios, northern peatlands are likely to become a C source (Müller & Joos, 2021; Qiu et al., 2022), especially when also considering the impacts of other disturbances such as land use, fire and drainage (Frolking et al., 2011; Loisel et al., 2021).

5. Conclusions

Our machine learning approach reasonably estimated peat basal ages of northern peatlands. Our simulated regional peatland C stock and long-term carbon accumulation rate are consistent with the literature. We estimate that regional peatland C stocks are 396-421 Pg C depending on peatland coverage, and that the regional mean Holocene carbon accumulation rate has been $22.9 \text{ g C} \cdot \text{m}^{-2} \cdot \text{yr}^{-1}$. The PTEM simulated active layer depth agrees with multiple datasets, and thereby we reconstruct the permafrost development in peat from 15ka BP to 1990. Peat permafrost development generally started around 7ka BP, peaked during 3ka BP-1ka BP, and has stabilized since 1ka BP. The temporal dynamics of active layer depth and permafrost dynamics are generally consistent with the timing of the Holocene Thermal Maximum (~11ka-5ka BP), Neoglacial cooling (~7ka-2ka BP, various in different regions), the Medieval Climate Anomaly (~1ka-750a BP), the Little Ice Age (~550a-250a BP) and Anthropocene warming (since ~200a BP).

From the Medieval Climate Anomaly to Anthropocene warming, we have classified northern peatlands into three categories depending on the permafrost condition: the region that developed permafrost in the Little Ice Age and thawed in the Anthropocene, the persistent permafrost region, and the permafrost-free region. We found that peatland C fluxes respond to climate warming differently in these three regions. As the freeze-thaw and permafrost-free regions are warmer, Anthropocene climate warming enhances decomposition more than NPP and thereby the C sink capacity decreases or is lost. On the contrary, the colder permafrost region showed higher carbon accumulation rates under Anthropocene warming due to NPP increasing more than decomposition. Therefore, under future climate warming, the current permafrost region will likely switch to less permafrost or permafrost-free conditions, and the C sink capacity of peatlands will decrease.

Acknowledgments:

We thank Joe Melton for providing data and commenting on an earlier version of this paper. The research is supported by NSF projects # 1802832 and 1802825.

571 Data availability:

572 The data in this study can be accessed from Purdue University Research Repository: Zhao, B., Zhuang,
573 Q., Frohking, S. (2022). Modeling carbon accumulation and greenhouse gas emissions of northern
574 peatlands since the Holocene. Purdue University Research Repository. doi:10.4231/6647-C769.

575

576

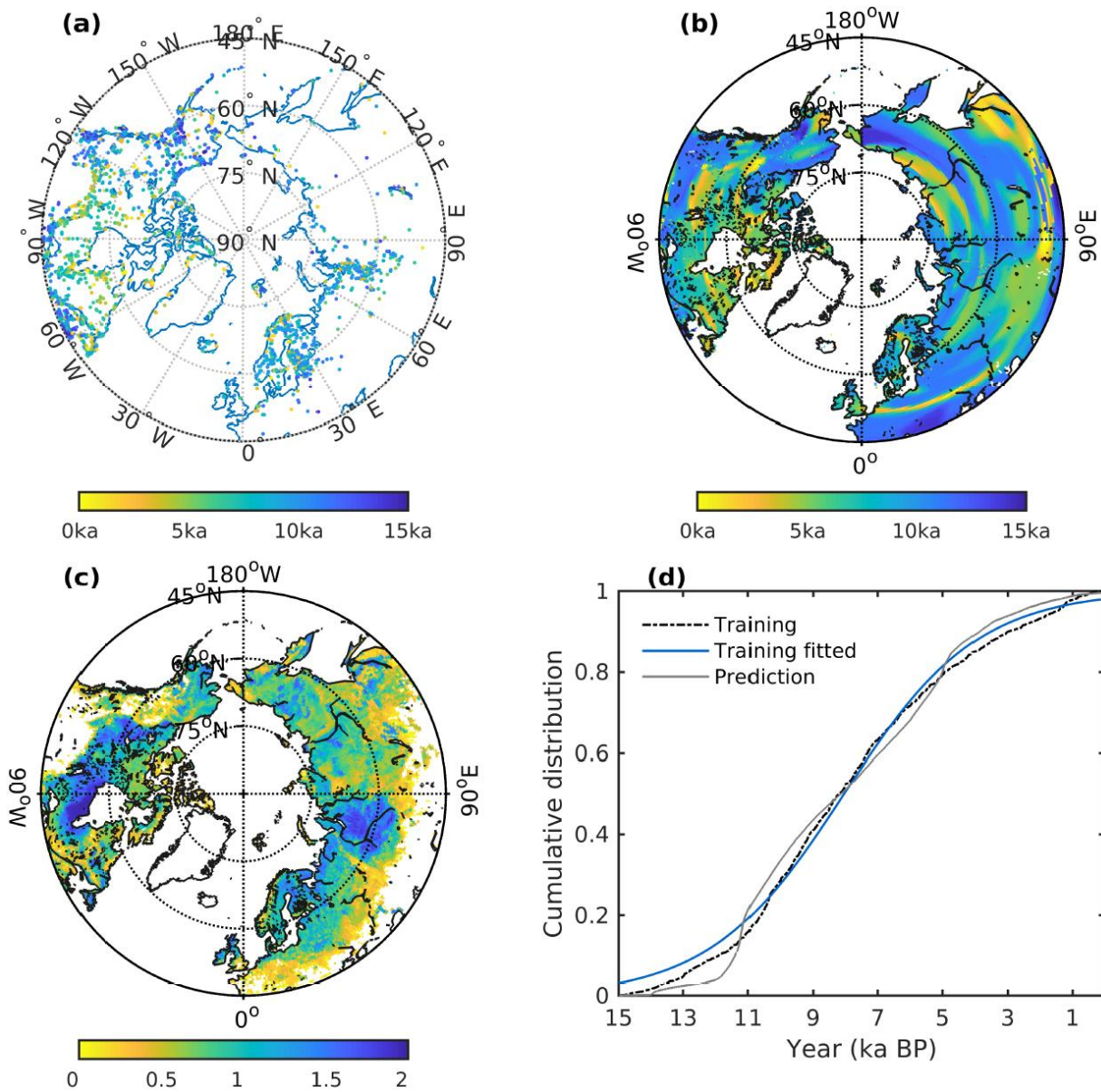
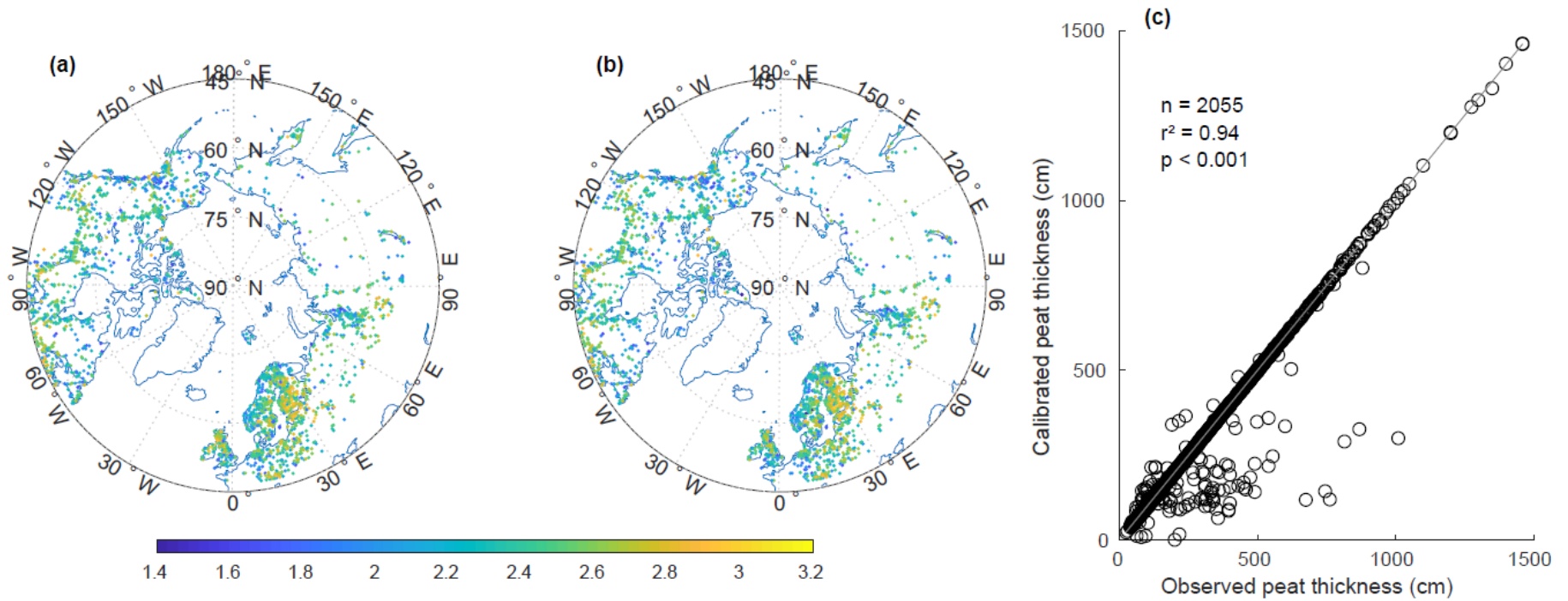


Figure 2. (a) The training basal dates of pan-Arctic peatlands (units: year BP); (b) the training and predicted basal dates of pan-Arctic peatlands (units: year BP); (c) log10 of the average peatland coverage percent, where grid cells with <1% peatland coverage are left blank; (d) cumulative distribution function (CDF) (0-1) of the training and predicted basal date dataset and the fitted line of the training CDF.



584

585 Figure 3. (a) Location and the log10 of observed peat thickness (log10(cm)) of the 2055 data points used for regional calibration. (b) Location
586 and the log10 of calibrated peat thickness (log10(cm)) of the same 2055 data points. (c) Comparison between the observed peat thickness and
587 calibrated peat thickness. The solid grey line is the 1: 1 line.

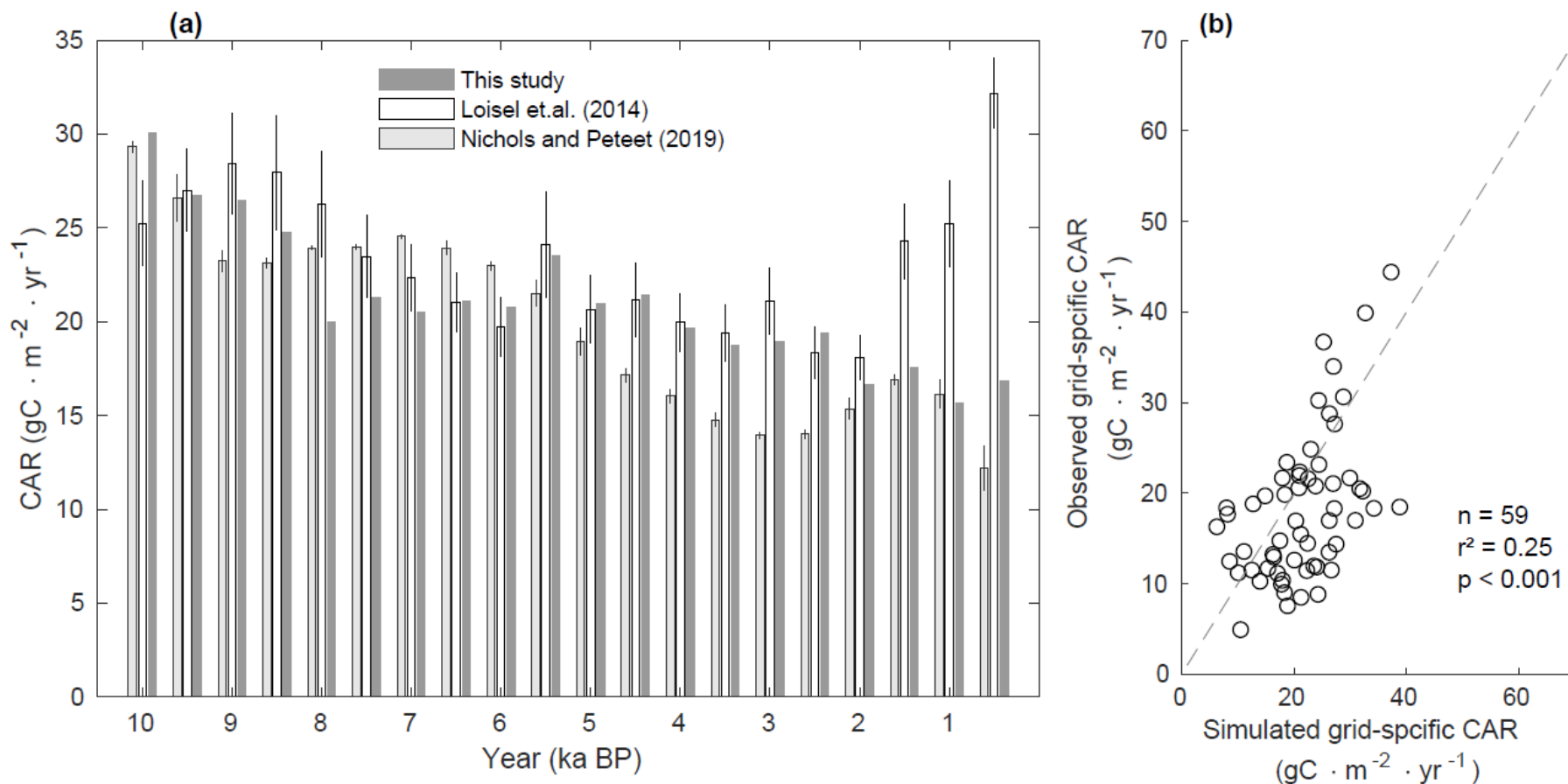


Figure 4. (a) Comparison of long-term C accumulation rate (CAR) from this study and the literature from 10ka BP to present in 500-yr bins. (b) Comparison between the long-term core-derived CAR (Loisel 2014) and simulated CAR in corresponding $0.5^{\circ} \times 0.5^{\circ}$ grids. The dash line is the 1: 1 line.

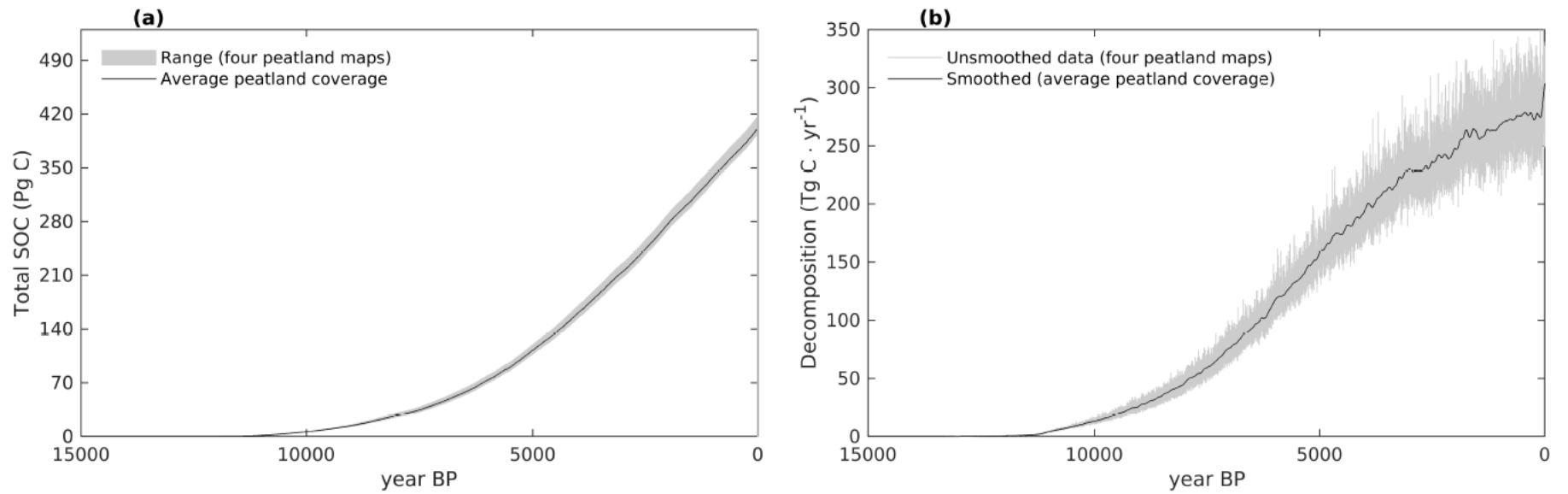
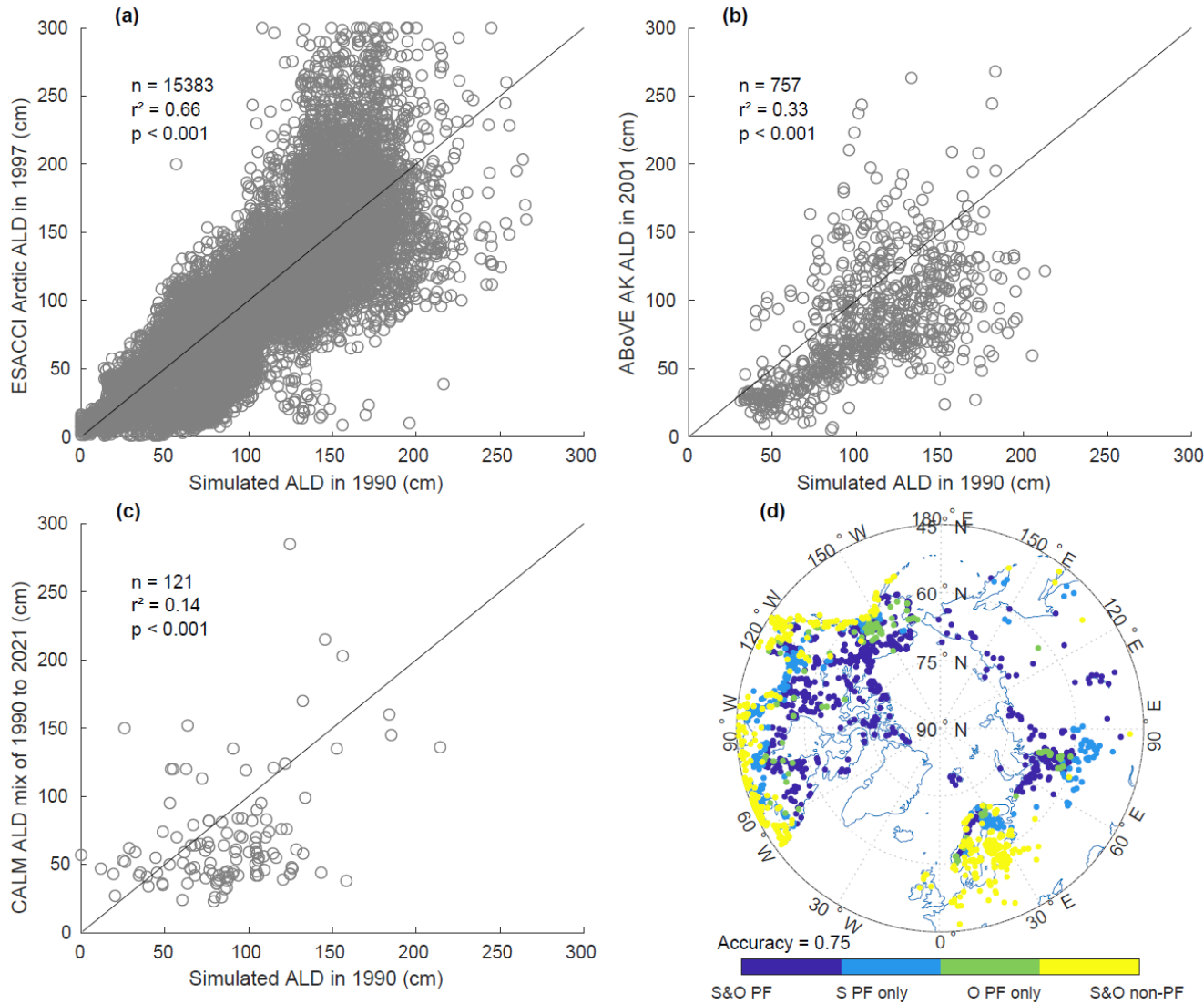


Figure 5. Time series of (a) pan-Arctic peatland C stocks; (b) pan-Arctic peatland C emissions from decomposition. The emissions of average peatland coverage in panel (b) are smoothed with Matlab's lowess function.



597

598 Figure 6. Comparison between simulated active layer depth (ALD) in 1990 and permafrost existence in peat in 1990 with the literature: (a)
 599 comparison with satellite-derived Arctic ALD 1997 (Obu et al., 2020); (b) comparison with satellite-derived Alaskan ALD in 2001 (Yi &
 600 Kimball, 2020); (c) comparison with ALD from CALM observation network (various years during 1990-2021) (Brown et al., 2000; Calm,
 601 1991-); (d) comparison with permafrost in peat record in core data. S&O PF indicates both simulation and observation have permafrost, S PF
 602 only indicates permafrost exist in only simulation, O PF only indicates permafrost exist in only observed core records, S&O non-PF indicates
 603 no permafrost existence in simulation or observed core data.

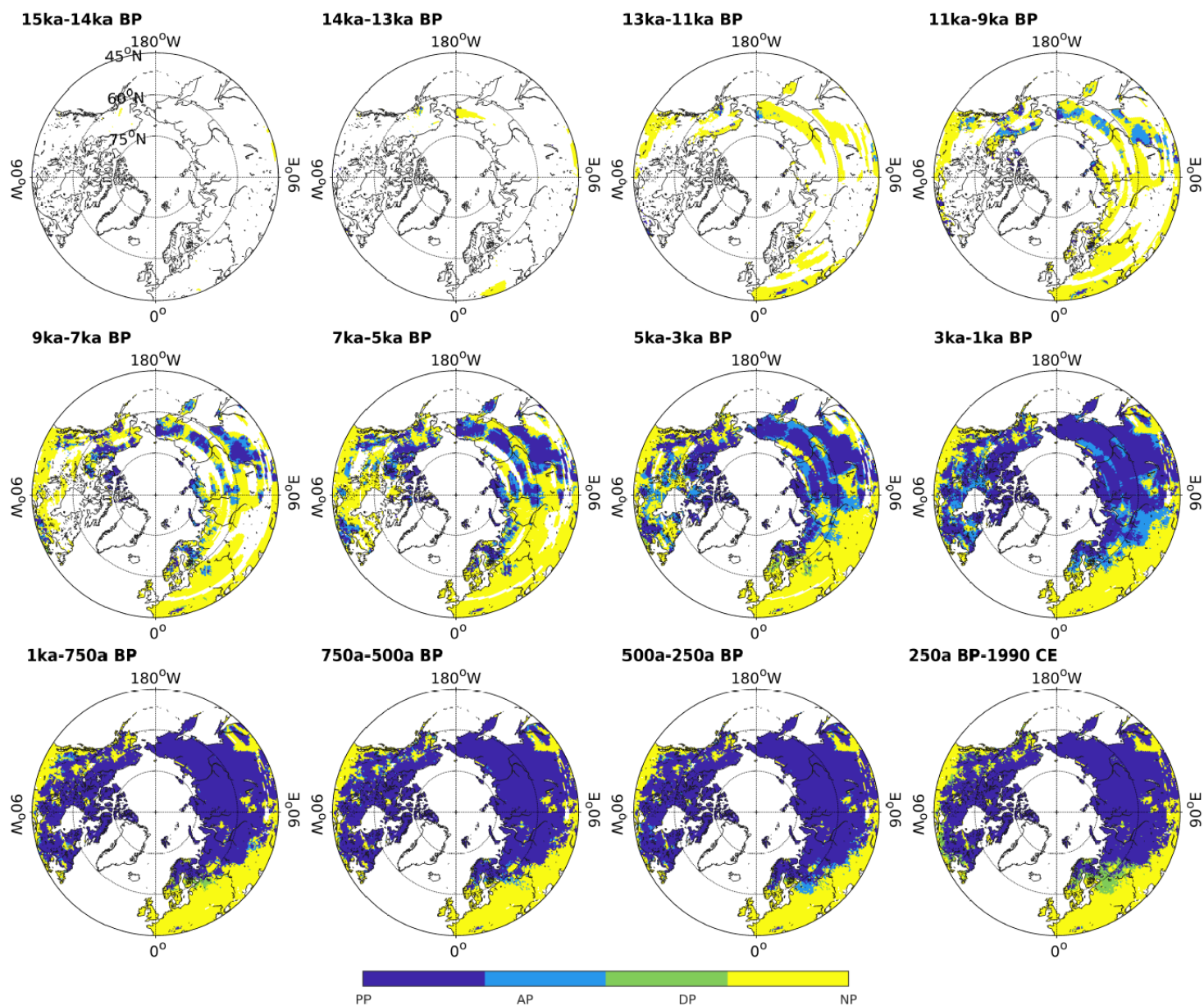
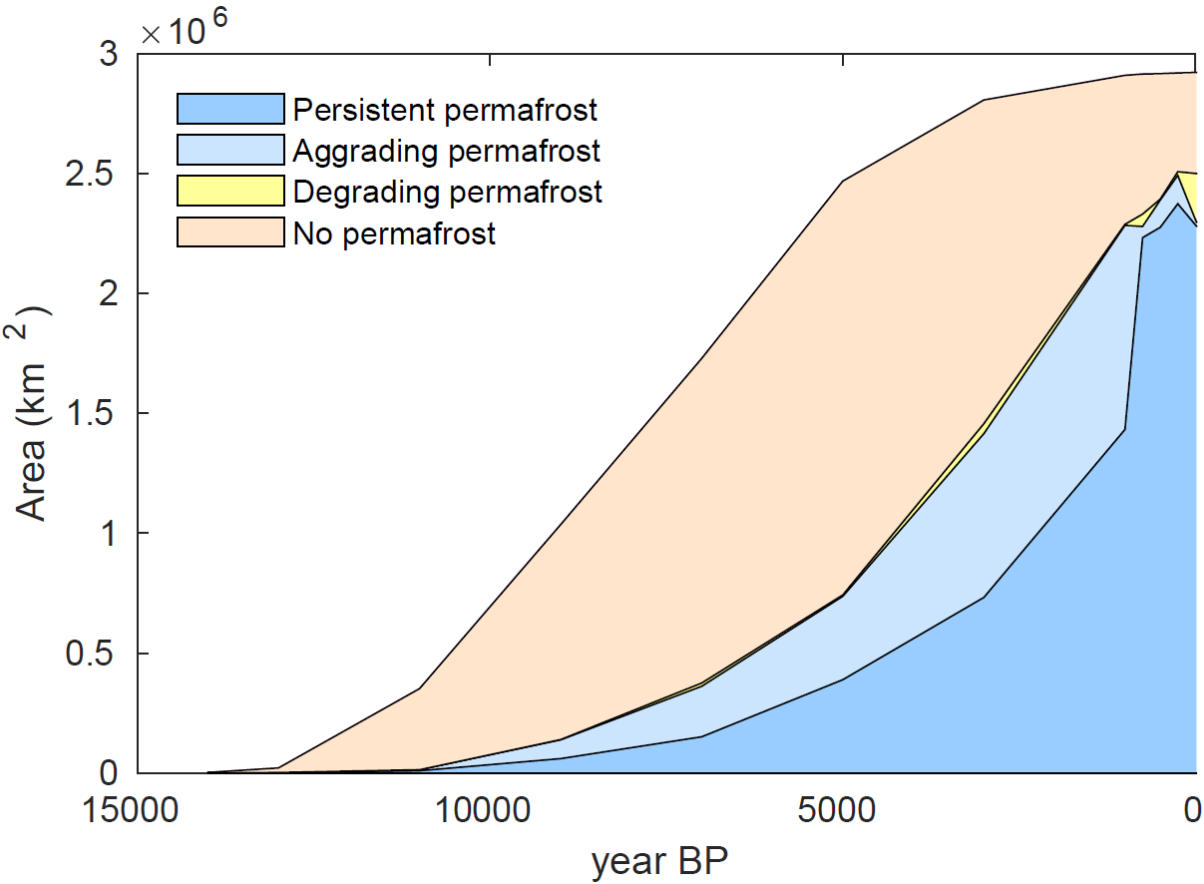


Figure 7. Permafrost dynamics in peatlands from 14ka BP to 1990CE. PP represents persistent permafrost, AP represents aggrading permafrost, DP represents degrading permafrost, and NP represents no permafrost.

607



608

609 Figure 8. The peatland area of persistent permafrost, aggrading permafrost, degrading permafrost and no
610 permafrost during 15ka BP-1990. The computed time interval is the same as Figure 7. The peatland coverage
611 is the average peatland coverage of estimates from Melton et al. (2022), Hugelius et al. (2020) and Xu et al.
612 (2018).

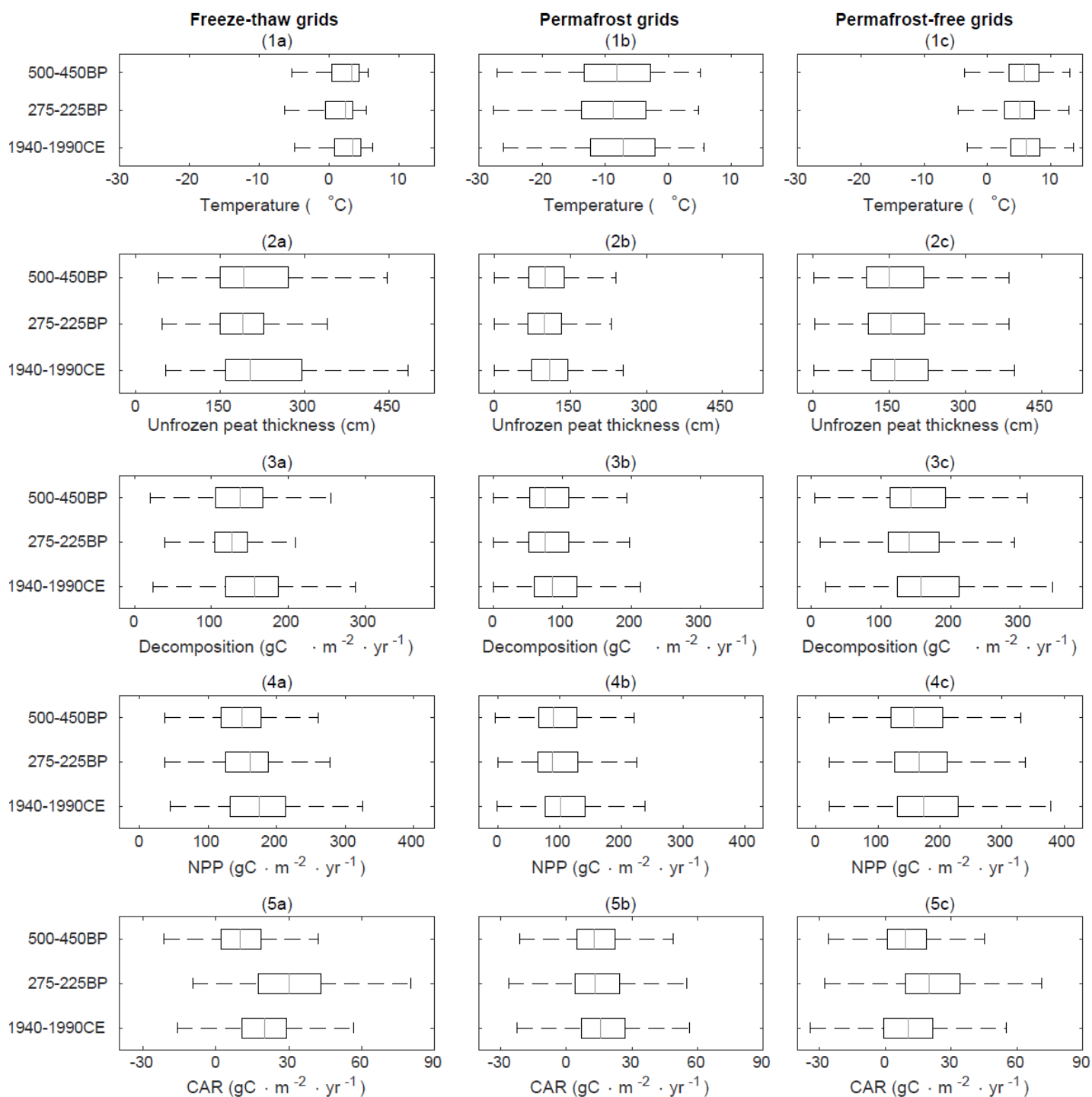


Figure 9. Temperature, unfrozen peat thickness, CH₄ emissions, CO₂ emissions, NPP and CAR of the grids that (a) permafrost formed during 500a BP-250a BP and thawed during 250a BP-1990CE; (b) permafrost persisted during 500a BP-1990CE; (c) permafrost did not exist during 500a BP-1990CE. The grey lines in the boxes are median values of the 50-year average values, box are interquartile range (25%-75%) values, and whiskers are the most extreme values not considered outliers.

620

Table 1 Comparison between regional peat C stocks and CAR

Regional SOC stocks (Pg C)	Source
397	This study (with Melton et al. (2022) peatland coverage)
421	This study (with Hugelius et al. (2020) peatland coverage)
396	This study (with Xu et al. (2018) peatland coverage)
404	This study (with average peatland coverage)
408	Qiu et al. (2019)
300	Hugelius et al. (2013) (Top soil 3m)
545-1045	Nichols and Peteet (2019)
400	Hugelius et al. (2020)
547	Yu et al. (2010)
436	Loisel et al. (2014)
365-550	Spahni et al. (2013)
351	Müller and Joos (2021)
455	Gorham (1991)
Holocene CAR (g C·m ⁻² yr ⁻¹)	
22.9	This study
22.9±2	Loisel et al. (2014)
18.6	Yu et al. (2009)
19.7-50.5	Nichols and Peteet (2019)
21.4	Chaudhary et al. (2020)
17.3-26.1	Turunen et al. (2002)
14.2-23.2	Treat, Jones, et al. (2016a)

621

622

623

624

References

- Allen, M. R., Dube, O. P., Solecki, W., Aragón-Durand, F., W. Cramer, S. H., Kainuma, M., et al. Zickfeld, K. (2018). *Framing and context. In: Global warming of 1.5°C. An ipcc special report on the impacts of global warming of 1.5°C above pre-industrial levels and related global greenhouse gas emission pathways, in the context of strengthening the global response to the threat of climate change, sustainable development, and efforts to eradicate poverty.*
- Brown, J., Hinkel, K. M., & Nelson, F. E. (2000). The circumpolar active layer monitoring (calm) program: Research designs and initial results. *Polar Geography*, 24(3), 166-258. Retrieved from <https://doi.org/10.1080/10889370009377698>. doi:10.1080/10889370009377698
- Calm. (1991-). Circumpolar active layer monitoring network-calm: Long-term observations of the climate-active layer-permafrost system.
- Chaudhary, N., Miller, P. A., & Smith, B. (2017). Modelling past, present and future peatland carbon accumulation across the pan-arctic region. *Biogeosciences*, 14(18), 4023-4044. Retrieved from <https://www.biogeosciences.net/14/4023/2017/>. doi:10.5194/bg-14-4023-2017
- Chaudhary, N., Westermann, S., Lamba, S., Shurpali, N., Sannel, A. B. K., Schurgers, G., et al. Smith, B. (2020). Modelling past and future peatland carbon dynamics across the pan-arctic. *Global Change Biology*, n/a(n/a). Retrieved from <https://doi.org/10.1111/gcb.15099>. doi:10.1111/gcb.15099
- Cheremisinoff, N. P. (1997). Groundwater remediation and treatment technologies. In N. P. Cheremisinoff (Ed.), (pp. vi). Westwood, NJ: William Andrew Publishing.
- Curiel Yuste, J., Baldocchi, D. D., Gershenson, A., Goldstein, A., Misson, L., & Wong, S. (2007). Microbial soil respiration and its dependency on carbon inputs, soil temperature and moisture. *Global Change Biology*, 13(9), 2018-2035. Retrieved from <https://doi.org/10.1111/j.1365-2486.2007.01415.x>. doi:<https://doi.org/10.1111/j.1365-2486.2007.01415.x>
- Czerniawska, J., & Chlachula, J. (2020). Climate-change induced permafrost degradation in yakutia, east siberia. *ARCTIC*, 73, 509-528. doi:10.14430/arctic71674
- Fan, Y., Li, H., & Miguez-Macho, G. (2013). Global patterns of groundwater table depth. *Science*, 339(6122), 940. Retrieved from <http://science.sciencemag.org/content/339/6122/940.abstract>. doi:10.1126/science.1229881
- Fao/Unesco. (1974). *Soil map of the world*. Retrieved from Paris:
- Frolking, S., Roulet, N. T., Tuittila, E., Bubier, J. L., Quillet, A., Talbot, J., & Richard, P. J. H. (2010). A new model of holocene peatland net primary production, decomposition, water balance, and peat accumulation. *Earth Syst. Dynam.*, 1(1), 1-21. Retrieved from <https://www.earth-syst-dynam.net/1/1/2010/>. doi:10.5194/esd-1-1-2010
- Frolking, S., Talbot, J., Jones, M. C., Treat, C. C., Kauffman, J. B., Tuittila, E.-S., & Roulet, N. (2011). Peatlands in the earth's 21st century climate system. *Environmental Reviews*, 19(NA), 371-396. Retrieved from <https://cdnsienc epub.com/doi/abs/10.1139/a11-014> doi:10.1139/a11-014
- Gallego-Sala, A. V., Charman, D. J., Brewer, S., Page, S. E., Prentice, I. C., Friedlingstein, P., et al. Zhao, Y. (2018). Latitudinal limits to the predicted increase of the peatland carbon sink

- with warming. *Nature Climate Change*, 8(10), 907-913. Retrieved from <https://doi.org/10.1038/s41558-018-0271-1>. doi:10.1038/s41558-018-0271-1
- Gandois, L., Hoyt, A. M., Hatté, C., Jeanneau, L., Teisserenc, R., Liotaud, M., & Tananaev, N. (2019). Contribution of peatland permafrost to dissolved organic matter along a thaw gradient in north siberia. *Environmental Science & Technology*, 53(24), 14165-14174. Retrieved from <https://doi.org/10.1021/acs.est.9b03735>. doi:10.1021/acs.est.9b03735
- Gao, J., Feng, J., Zhang, X., Yu, F.-H., Xu, X., & Kuzyakov, Y. (2016). Drying-rewetting cycles alter carbon and nitrogen mineralization in litter-amended alpine wetland soil. *CATENA*, 145, 285-290. Retrieved from <https://www.sciencedirect.com/science/article/pii/S0341816216302314>. doi:<https://doi.org/10.1016/j.catena.2016.06.026>
- Gistemp-Team. (2021). *Giss surface temperature analysis (gistemp), version 4, nasa goddard institute for space studies*.
- Glaser, P. H., Siegel, D. I., Chanton, J. P., Reeve, A. S., Rosenberry, D. O., Corbett, J. E., et al. Levy, Z. (2016). Climatic drivers for multidecadal shifts in solute transport and methane production zones within a large peat basin. *Global Biogeochemical Cycles*, 30(11), 1578-1598. Retrieved from <http://pubs.er.usgs.gov/publication/70179639>. doi:10.1002/2016GB005397
- Gorham, E. (1991). Northern peatlands: Role in the carbon cycle and probable responses to climatic warming. *Ecological Applications*, 1(2), 182-195. Retrieved from <https://doi.org/10.2307/1941811>. doi:<https://doi.org/10.2307/1941811>
- Gorham, E., Lehman, C., Dyke, A., Janssens, J., & Dyke, L. (2007). Temporal and spatial aspects of peatland initiation following deglaciation in north america. *Quaternary Science Reviews*, 26(3), 300-311. Retrieved from <http://www.sciencedirect.com/science/article/pii/S0277379106002666>. doi:<https://doi.org/10.1016/j.quascirev.2006.08.008>
- Granberg, G., Grip, H., Löfvenius, M. O., Sundh, I., Svensson, B. H., & Nilsson, M. (1999). A simple model for simulation of water content, soil frost, and soil temperatures in boreal mixed mires. *Water Resources Research*, 35(12), 3771-3782. Retrieved from <https://doi.org/10.1029/1999WR900216>. doi:<https://doi.org/10.1029/1999WR900216>
- Griffiths, N. A., Sebestyen, S. D., & Oleheiser, K. C. (2019). Variation in peatland porewater chemistry over time and space along a bog to fen gradient. *Science of The Total Environment*, 697, 134152. Retrieved from <https://www.sciencedirect.com/science/article/pii/S0048969719341294>. doi:<https://doi.org/10.1016/j.scitotenv.2019.134152>
- He, F. (2011). *Simulating transient climate evolution of the last deglaciation with ccs3m3*. (Doctor of Philosophy), UNIVERSITY OF WISCONSIN-MADISON, Madison.
- Heffernan, L., Estop-Aragónés, C., Knorr, K.-H., Talbot, J., & Olefeldt, D. (2020). Long-term impacts of permafrost thaw on carbon storage in peatlands: Deep losses offset by surficial accumulation. *Journal of Geophysical Research: Biogeosciences*, 125(3), e2019JG005501. Retrieved from <https://doi.org/10.1029/2019JG005501>. doi:<https://doi.org/10.1029/2019JG005501>
- Huang, Y., Ciais, P., Luo, Y., Zhu, D., Wang, Y., Qiu, C., et al. Qu, L. (2021). Tradeoff of co2 and ch4 emissions from global peatlands under water-table drawdown. *Nature Climate Change*, 11(7), 618-622. Retrieved from <https://doi.org/10.1038/s41558-021-01059-w>. doi:10.1038/s41558-021-01059-w

- Hugelius, G., Bockheim, J. G., Camill, P., Elberling, B., Grosse, G., Harden, J. W., et al. Yu, Z. (2013). A new data set for estimating organic carbon storage to 3 m depth in soils of the northern circumpolar permafrost region. *Earth Syst. Sci. Data*, 5(2), 393-402. Retrieved from <https://essd.copernicus.org/articles/5/393/2013/>. doi:10.5194/essd-5-393-2013
- Hugelius, G., Loisel, J., Chadburn, S., Jackson, R. B., Jones, M., Macdonald, G., et al. Yu, Z. (2020). Large stocks of peatland carbon and nitrogen are vulnerable to permafrost thaw. *Proceedings of the National Academy of Sciences*, 117(34), 20438. Retrieved from <http://www.pnas.org/content/117/34/20438.abstract>. doi:10.1073/pnas.1916387117
- Ipcc. (2007). *Climate change 2007: The physical science basis. Contribution of working group i to the fourth assessment report of the intergovernmental panel on climate change*. Retrieved from Cambridge, United Kingdom and New York, NY, USA:
- Jones, M. C., Harden, J., O'donnell, J., Manies, K., Jorgenson, T., Treat, C., & Ewing, S. (2017). Rapid carbon loss and slow recovery following permafrost thaw in boreal peatlands. *Global Change Biology*, 23(3), 1109-1127. Retrieved from <https://doi.org/10.1111/gcb.13403>. doi:<https://doi.org/10.1111/gcb.13403>
- Kaufman, D., McKay, N., Routson, C., Erb, M., Dätwyler, C., Sommer, P. S., et al. Davis, B. (2020). Holocene global mean surface temperature, a multi-method reconstruction approach. *Scientific Data*, 7(1), 201. Retrieved from <https://doi.org/10.1038/s41597-020-0530-7>. doi:10.1038/s41597-020-0530-7
- Koerselman, W., Van Kerkhoven, M. B., & Verhoeven, J. T. (1993). Release of inorganic n, p and k in peat soils; effect of temperature, water chemistry and water level. *Biogeochemistry*, 20(2), 63-81. Retrieved from <https://doi.org/10.1007/BF00004135>. doi:10.1007/BF00004135
- Korhola, A., Ruppel, M., Seppä, H., Välranta, M., Virtanen, T., & Weckström, J. (2010). The importance of northern peatland expansion to the late-holocene rise of atmospheric methane. *Quaternary Science Reviews*, 29(5), 611-617. Retrieved from <http://www.sciencedirect.com/science/article/pii/S0277379109004235>. doi:<https://doi.org/10.1016/j.quascirev.2009.12.010>
- Limpens, J., Heijmans, M. M. P. D., & Berendse, F. (2006). The nitrogen cycle in boreal peatlands. In R. K. Wieder & D. H. Vitt (Eds.), *Boreal peatland ecosystems* (pp. 195-230). Berlin, Heidelberg: Springer Berlin Heidelberg.
- Loisel, J., Gallego-Sala, A. V., Amesbury, M. J., Magnan, G., Anshari, G., Beilman, D. W., et al. Wu, J. (2021). Expert assessment of future vulnerability of the global peatland carbon sink. *Nature Climate Change*, 11(1), 70-77. Retrieved from <https://doi.org/10.1038/s41558-020-00944-0>. doi:10.1038/s41558-020-00944-0
- Loisel, J., Van Bellen, S., Pelletier, L., Talbot, J., Hugelius, G., Karan, D., et al. Holmquist, J. (2017). Insights and issues with estimating northern peatland carbon stocks and fluxes since the last glacial maximum. *Earth-Science Reviews*, 165, 59-80. Retrieved from <https://www.sciencedirect.com/science/article/pii/S0012825216304524>. doi:<https://doi.org/10.1016/j.earscirev.2016.12.001>
- Loisel, J., Yu, Z., Beilman, D. W., Camill, P., Alm, J., Amesbury, M. J., et al. Zhou, W. (2014). A database and synthesis of northern peatland soil properties and holocene carbon and nitrogen accumulation. *The Holocene*, 24(9), 1028-1042. Retrieved from <https://doi.org/10.1177/0959683614538073>. doi:10.1177/0959683614538073
- López-Blanco, E., Jackowicz-Korczynski, M., Mastepanov, M., Skov, K., Westergaard-Nielsen, A., Williams, M., & Christensen, T. R. (2020). Multi-year data-model evaluation reveals

- the importance of nutrient availability over climate in arctic ecosystem c dynamics. *Environmental Research Letters*, 15(9), 094007. Retrieved from <http://dx.doi.org/10.1088/1748-9326/ab865b>. doi:10.1088/1748-9326/ab865b
- Luo, D., Wu, Q., Jin, H., Marchenko, S. S., Lü, L., & Gao, S. (2016). Recent changes in the active layer thickness across the northern hemisphere. *Environmental Earth Sciences*, 75(7), 555. Retrieved from <https://doi.org/10.1007/s12665-015-5229-2>. doi:10.1007/s12665-015-5229-2
- Lupascu, M., Wadham, J. L., Hornibrook, E. R. C., & Pancost, R. D. (2012). Temperature sensitivity of methane production in the permafrost active layer at stordalen, sweden: A comparison with non-permafrost northern wetlands. *Arctic, Antarctic, and Alpine Research*, 44(4), 469-482. Retrieved from <https://doi.org/10.1657/1938-4246-44.4.469>. doi:10.1657/1938-4246-44.4.469
- Macdonald, G. M., Beilman, D. W., Kremenetski, K. V., Sheng, Y., Smith, L. C., & Velichko, A. A. (2006). Rapid early development of circumarctic peatlands and atmospheric ch₄ and co₂ variations. *Science*, 314(5797), 285. Retrieved from <http://science.sciencemag.org/content/314/5797/285.abstract>. doi:10.1126/science.1131722
- Mann Michael, E., Zhang, Z., Rutherford, S., Bradley Raymond, S., Hughes Malcolm, K., Shindell, D., et al. Ni, F. (2009). Global signatures and dynamical origins of the little ice age and medieval climate anomaly. *Science*, 326(5957), 1256-1260. Retrieved from <https://doi.org/10.1126/science.1177303>. doi:10.1126/science.1177303
- Mccalley, C. K., Woodcroft, B. J., Hodgkins, S. B., Wehr, R. A., Kim, E.-H., Mondav, R., et al. Saleska, S. R. (2014). Methane dynamics regulated by microbial community response to permafrost thaw. *Nature*, 514(7523), 478-481. Retrieved from <https://doi.org/10.1038/nature13798>. doi:10.1038/nature13798
- Mcguire, A. D., Lawrence, D. M., Koven, C., Clein, J. S., Burke, E., Chen, G., et al. Zhuang, Q. (2018). Dependence of the evolution of carbon dynamics in the northern permafrost region on the trajectory of climate change. *Proceedings of the National Academy of Sciences*, 115(15), 3882. Retrieved from <http://www.pnas.org/content/115/15/3882.abstract>. doi:10.1073/pnas.1719903115
- Mckay, N. P., Kaufman, D. S., Routson, C. C., Erb, M. P., & Zander, P. D. (2018). The onset and rate of holocene neoglacial cooling in the arctic. *Geophysical Research Letters*, 45(22), 12,487-412,496. Retrieved from <https://doi.org/10.1029/2018GL079773>. doi:<https://doi.org/10.1029/2018GL079773>
- Melton, J. R., Chan, E., Millard, K., Fortier, M., Winton, R. S., Martín-López, J. M., et al. Verchot, L. V. (2022). A map of global peatland extent created using machine learning (peat-ml). *Geosci. Model Dev. Discuss.*, 2022, 1-44. Retrieved from <https://gmd.copernicus.org/preprints/gmd-2021-426/>. doi:10.5194/gmd-2021-426
- Müller, J., & Joos, F. (2021). Committed and projected future changes in global peatlands – continued transient model simulations since the last glacial maximum. *Biogeosciences*, 18(12), 3657-3687. Retrieved from <https://bg.copernicus.org/articles/18/3657/2021/>. doi:10.5194/bg-18-3657-2021
- Nichols, J. E., & Peteet, D. M. (2019). Rapid expansion of northern peatlands and doubled estimate of carbon storage. *Nature Geoscience*, 12(11), 917-921. Retrieved from <https://doi.org/10.1038/s41561-019-0454-z>. doi:10.1038/s41561-019-0454-z

- O'donnell, J. A., Jorgenson, M. T., Harden, J. W., Mcguire, A. D., Kanevskiy, M. Z., & Wickland, K. P. (2012). The effects of permafrost thaw on soil hydrologic, thermal, and carbon dynamics in an alaskan peatland. *Ecosystems*, 15(2), 213-229. Retrieved from <https://doi.org/10.1007/s10021-011-9504-0>. doi:10.1007/s10021-011-9504-0
- Obu, J., Westermann, S., Barboux, C., Bartsch, A., Delaloye, R., Grosse, G., et al. Wiesmann, A. (2020). *Esa permafrost climate change initiative (permafrost_cci): Permafrost climate research data package v1*.
- Ojanen, P., Penttilä, T., Tolvanen, A., Hotanen, J.-P., Saarimaa, M., Nousiainen, H., & Minkkinen, K. (2019). Long-term effect of fertilization on the greenhouse gas exchange of low-productive peatland forests. *Forest Ecology and Management*, 432, 786-798. Retrieved from <https://www.sciencedirect.com/science/article/pii/S0378112718311733>. doi:<https://doi.org/10.1016/j.foreco.2018.10.015>
- Olefeldt, D., Hovemyr, M., Kuhn, M. A., Bastviken, D., Bohn, T. J., Connolly, J., et al. Watts, J. D. (2021). The boreal–arctic wetland and lake dataset (bawld). *Earth Syst. Sci. Data*, 13(11), 5127-5149. Retrieved from <https://essd.copernicus.org/articles/13/5127/2021/>. doi:10.5194/essd-13-5127-2021
- Palmer, M. D., Harris, G. R., & Gregory, J. M. (2018). Extending cmip5 projections of global mean temperature change and sea level rise due to thermal expansion using a physically-based emulator. *Environmental Research Letters*, 13(8), 084003. Retrieved from <http://dx.doi.org/10.1088/1748-9326/aad2e4>. doi:10.1088/1748-9326/aad2e4
- Pedregosa, F., Varoquaux, G., Gramfort, A., Michel, V., Thirion, B., Grisel, O., et al. Duchesnay, É. (2011). Scikit-learn: Machine learning in python. *J. Mach. Learn. Res.*, 12(null), 2825–2830.
- Peng, X., Zhang, T., Frauenfeld, O. W., Wang, S., Qiao, L., Du, R., & Mu, C. (2020). Northern hemisphere greening in association with warming permafrost. *Journal of Geophysical Research: Biogeosciences*, 125(1), e2019JG005086. Retrieved from <https://doi.org/10.1029/2019JG005086>. doi:<https://doi.org/10.1029/2019JG005086>
- Plaza, C., Pegoraro, E., Bracho, R., Celis, G., Crummer, K. G., Hutchings, J. A., et al. Schuur, E. a. G. (2019). Direct observation of permafrost degradation and rapid soil carbon loss in tundra. *Nature Geoscience*, 12(8), 627-631. Retrieved from <https://doi.org/10.1038/s41561-019-0387-6>. doi:10.1038/s41561-019-0387-6
- Qiu, C., Ciais, P., Zhu, D., Guenet, B., Chang, J., Chaudhary, N., et al. Westermann, S. (2022). A strong mitigation scenario maintains climate neutrality of northern peatlands. *One Earth*. Retrieved from <https://www.sciencedirect.com/science/article/pii/S2590332221007260>. doi:<https://doi.org/10.1016/j.oneear.2021.12.008>
- Qiu, C., Ciais, P., Zhu, D., Guenet, B., Peng, S., Petrescu, A. M. R., et al. Brewer, S. C. (2021). Large historical carbon emissions from cultivated northern peatlands. *Science Advances*, 7(23), eabf1332. Retrieved from <https://www.science.org/doi/abs/10.1126/sciadv.abf1332> doi:doi:10.1126/sciadv.abf1332
- Qiu, C., Zhu, D., Ciais, P., Guenet, B., & Peng, S. (2020). The role of northern peatlands in the global carbon cycle for the 21st century. *Global Ecology and Biogeography*, 29(5), 956-973. Retrieved from <https://doi.org/10.1111/geb.13081>. doi:<https://doi.org/10.1111/geb.13081>
- Qiu, C., Zhu, D., Ciais, P., Guenet, B., Peng, S., Krinner, G., et al. Hastie, A. (2019). Modelling northern peatland area and carbon dynamics since the holocene with the orchidee-peat

- land surface model (svn r5488). *Geosci. Model Dev.*, 12(7), 2961-2982. Retrieved from <https://gmd.copernicus.org/articles/12/2961/2019/>. doi:10.5194/gmd-12-2961-2019
- Song, Y., Song, C., Ren, J., Tan, W., Jin, S., & Jiang, L. (2018). Influence of nitrogen additions on litter decomposition, nutrient dynamics, and enzymatic activity of two plant species in a peatland in northeast china. *Science of The Total Environment*, 625, 640-646. Retrieved from <https://www.sciencedirect.com/science/article/pii/S0048969717337440>. doi:<https://doi.org/10.1016/j.scitotenv.2017.12.311>
- Spahni, R., Joos, F., Stocker, B. D., Steinacher, M., & Yu, Z. C. (2013). Transient simulations of the carbon and nitrogen dynamics in northern peatlands: From the last glacial maximum to the 21st century. *Clim. Past*, 9(3), 1287-1308. Retrieved from <https://cp.copernicus.org/articles/9/1287/2013/>. doi:10.5194/cp-9-1287-2013
- Stocker, B. D., Spahni, R., & Joos, F. (2014). Dyptop: A cost-efficient topmodel implementation to simulate sub-grid spatio-temporal dynamics of global wetlands and peatlands. *Geosci. Model Dev.*, 7(6), 3089-3110. Retrieved from <https://gmd.copernicus.org/articles/7/3089/2014/>. doi:10.5194/gmd-7-3089-2014
- Treat, C. C., & Jones, M. C. (2018). Near-surface permafrost aggradation in northern hemisphere peatlands shows regional and global trends during the past 6000 years. *The Holocene*, 28(6), 998-1010. Retrieved from <https://doi.org/10.1177/0959683617752858>. doi:10.1177/0959683617752858
- Treat, C. C., Jones, M. C., Alder, J., Sannel, A. B. K., Camill, P., & Frolking, S. (2021). Predicted vulnerability of carbon in permafrost peatlands with future climate change and permafrost thaw in western canada. *Journal of Geophysical Research: Biogeosciences*, n/a(n/a), e2020JG005872. Retrieved from <https://doi.org/10.1029/2020JG005872>. doi:<https://doi.org/10.1029/2020JG005872>
- Treat, C. C., Jones, M. C., Brosius, L., Grosse, G., Walter Anthony, K., & Frolking, S. (2021). The role of wetland expansion and successional processes in methane emissions from northern wetlands during the holocene. *Quaternary Science Reviews*, 257, 106864. Retrieved from <https://www.sciencedirect.com/science/article/pii/S0277379121000718>. doi:<https://doi.org/10.1016/j.quascirev.2021.106864>
- Treat, C. C., Jones, M. C., Brosius, L. S., Grosse, G., & Walter Anthony, K. M. (2016). *Radiocarbon dates of peatland initiation across the northern high latitudes*. Retrieved from: <https://doi.org/10.1594/PANGAEA.864101>
- Treat, C. C., Jones, M. C., Camill, P., Gallego-Sala, A., Garneau, M., Harden, J. W., et al. Välranta, M. (2016a). Effects of permafrost aggradation on peat properties as determined from a pan-arctic synthesis of plant macrofossils. *Journal of Geophysical Research: Biogeosciences*, 121(1), 78-94. Retrieved from <https://doi.org/10.1002/2015JG003061>. doi:<https://doi.org/10.1002/2015JG003061>
- Treat, C. C., Jones, M. C., Camill, P., Gallego-Sala, A., Garneau, M., Harden, J. W., et al. Välranta, M. (2016b). *Synthesis dataset of physical and ecosystem properties from pan-arctic wetland sites using peat core analysis*.
- Treat, C. C., Jones, M. C., Camill, P., Gallego-Sala, A. V., Garneau, M., Harden, J. W., et al. Välranta, M. (2016c) Synthesis dataset of physical and ecosystem properties from pan-arctic wetland sites using peat core analysis. In. *Supplement to: Treat, CC et al. (2016): Effects of permafrost aggradation on peat properties as determined from a pan-Arctic synthesis of plant macrofossils. Journal of Geophysical Research: Biogeosciences*, 121(1), 78-94, <https://doi.org/10.1002/2015JG003061>: PANGAEA.

- Turetsky, M. R., Benscoter, B., Page, S., Rein, G., Van Der Werf, G. R., & Watts, A. (2015). Global vulnerability of peatlands to fire and carbon loss. *Nature Geoscience*, 8(1), 11-14. Retrieved from <https://doi.org/10.1038/ngeo2325>. doi:10.1038/ngeo2325
- Turetsky, M. R., Wieder, R. K., & Vitt, D. H. (2002). Boreal peatland c fluxes under varying permafrost regimes. *Soil Biology and Biochemistry*, 34(7), 907-912. Retrieved from <http://www.sciencedirect.com/science/article/pii/S0038071702000226>. doi:[https://doi.org/10.1016/S0038-0717\(02\)00022-6](https://doi.org/10.1016/S0038-0717(02)00022-6)
- Turunen, J., Tomppo, E., Tolonen, K., & Reinikainen, A. (2002). Estimating carbon accumulation rates of undrained mires in finland—application to boreal and subarctic regions. *The Holocene*, 12(1), 69-80. Retrieved from <https://doi.org/10.1191/0959683602hl522rp>. doi:10.1191/0959683602hl522rp
- Weiss, R., Shurpali, N., Sallantausta, T., Laiho, R., Laine, J., & Alm, J. (2006). Simulation of water table level and peat temperatures in boreal peatlands. *ECOLOGICAL MODELLING*, 192, 441-456. doi:10.1016/j.ecolmodel.2005.07.016
- Xu, J., Morris, P. J., Liu, J., & Holden, J. (2018). Peatmap: Refining estimates of global peatland distribution based on a meta-analysis. *CATENA*, 160, 134-140. Retrieved from <https://www.sciencedirect.com/science/article/pii/S0341816217303004>. doi:<https://doi.org/10.1016/j.catena.2017.09.010>
- Yi, Y., & Kimball, J. S. (2020). Above: Active layer thickness from remote sensing permafrost model, alaska, 2001-2015. In: ORNL Distributed Active Archive Center.
- Young, D. M., Baird, A. J., Charman, D. J., Evans, C. D., Gallego-Sala, A. V., Gill, P. J., et al. Swindles, G. T. (2019). Misinterpreting carbon accumulation rates in records from near-surface peat. *Scientific Reports*, 9(1), 17939. Retrieved from <https://doi.org/10.1038/s41598-019-53879-8>. doi:10.1038/s41598-019-53879-8
- Yu, Z., Beilman, D., & Jones, M. (2009). Sensitivity of northern peatland carbon dynamics to holocene climate change. *Washington DC American Geophysical Union Geophysical Monograph Series*, 184, 55-69. doi:10.1029/2008GM000822
- Yu, Z., Loisel, J., Brosseau, D. P., Beilman, D. W., & Hunt, S. J. (2010). Global peatland dynamics since the last glacial maximum. *Geophysical Research Letters*, 37(13). Retrieved from <https://agupubs.onlinelibrary.wiley.com/doi/abs/10.1029/2010GL043584>. doi:<https://doi.org/10.1029/2010GL043584>
- Zhang, H., Gallego-Sala, A. V., Amesbury, M. J., Charman, D. J., Piilo, S. R., & Väliranta, M. M. (2018). Inconsistent response of arctic permafrost peatland carbon accumulation to warm climate phases. *Global Biogeochemical Cycles*, 32(10), 1605-1620. Retrieved from <https://doi.org/10.1029/2018GB005980>. doi:<https://doi.org/10.1029/2018GB005980>
- Zhao, B., Zhuang, Q., Treat, C., & Froking, S. (2022). A model intercomparison analysis for controls on c accumulation in north american peatlands. *Journal of Geophysical Research: Biogeosciences*, 127(5), e2021JG006762. Retrieved from <https://doi.org/10.1029/2021JG006762>. doi:<https://doi.org/10.1029/2021JG006762>
- Zhuang, Q., Mcguire, A. D., O'Neill, K. P., Harden, J. W., Romanovsky, V. E., & Yarie, J. (2002). Modeling soil thermal and carbon dynamics of a fire chronosequence in interior alaska. *Journal of Geophysical Research: Atmospheres*, 107(D1), FFR 3-1-FFR 3-26. Retrieved from <https://doi.org/10.1029/2001JD001244>. doi:<https://doi.org/10.1029/2001JD001244>
- Zhuang, Q., Melillo, J. M., Kicklighter, D. W., Prinn, R. G., Mcguire, A. D., Steudler, P. A., et al. Hu, S. (2004). Methane fluxes between terrestrial ecosystems and the atmosphere at

- northern high latitudes during the past century: A retrospective analysis with a process-based biogeochemistry model. *Global Biogeochemical Cycles*, 18(3). Retrieved from <https://doi.org/10.1029/2004GB002239>. doi:<https://doi.org/10.1029/2004GB002239>
- Zhuang, Q., Romanovsky, V., & McGuire, A. (2001). Incorporation of a permafrost model into a large-scale ecosystem model: Evaluation of temporal and spatial scaling issues in simulating soil thermal dynamics. *Journal of Geophysical Research*, 106, 33649-33670. doi:10.1029/2001JD900151
- Zhuang, Q., Wang, S., Zhao, B., Aires, F., Prigent, C., Yu, Z., et al. Bridgham, S. (2020). Modeling holocene peatland carbon accumulation in north america. *Journal of Geophysical Research: Biogeosciences*, 125(11), e2019JG005230. Retrieved from <https://doi.org/10.1029/2019JG005230>. doi:<https://doi.org/10.1029/2019JG005230>

Supporting References

- ecosystem [and discussion]. *Philosophical Transactions of the Royal Society of London. Series B, Biological Sciences*, 305(1124), 487-499. Retrieved from <http://www.jstor.org/stable/2396100>.
- Fan, Y., Li, H., & Miguez-Macho, G. (2013). Global patterns of groundwater table depth. *Science*, 339(6122), 940. Retrieved from <http://science.sciencemag.org/content/339/6122/940.abstract>. doi:10.1126/science.1229881
- Granberg, G., Grip, H., Löfvenius, M. O., Sundh, I., Svensson, B. H., & Nilsson, M. (1999). A simple model for simulation of water content, soil frost, and soil temperatures in boreal mixed mires. *Water Resources Research*, 35(12), 3771-3782. Retrieved from <https://doi.org/10.1029/1999WR900216>. doi:<https://doi.org/10.1029/1999WR900216>
- Hugelius, G., Bockheim, J. G., Camill, P., Elberling, B., Grosse, G., Harden, J. W., et al. Yu, Z. (2013). A new data set for estimating organic carbon storage to 3 m depth in soils of the northern circumpolar permafrost region. *Earth Syst. Sci. Data*, 5(2), 393-402. Retrieved from <https://essd.copernicus.org/articles/5/393/2013/>. doi:10.5194/essd-5-393-2013
- Hugelius, G., Loisel, J., Chadburn, S., Jackson, R. B., Jones, M., Macdonald, G., et al. Yu, Z. (2020). Large stocks of peatland carbon and nitrogen are vulnerable to permafrost thaw. *Proceedings of the National Academy of Sciences*, 117(34), 20438. Retrieved from <http://www.pnas.org/content/117/34/20438.abstract>. doi:10.1073/pnas.1916387117
- Koerselman, W., Van Kerkhoven, M. B., & Verhoeven, J. T. (1993). Release of inorganic n, p and k in peat soils; effect of temperature, water chemistry and water level. *Biogeochemistry*, 20(2), 63-81. Retrieved from <https://doi.org/10.1007/BF00004135>. doi:10.1007/BF00004135
- López-Blanco, E., Jackowicz-Korczynski, M., Mastepanov, M., Skov, K., Westergaard-Nielsen, A., Williams, M., & Christensen, T. R. (2020). Multi-year data-model evaluation reveals the importance of nutrient availability over climate in arctic ecosystem c dynamics. *Environmental Research Letters*, 15(9), 094007. Retrieved from <http://dx.doi.org/10.1088/1748-9326/ab865b>. doi:10.1088/1748-9326/ab865b
- López-Blanco, E., Lund, M., Williams, M., Tamstorf, M. P., Westergaard-Nielsen, A., Exbrayat, J. F., et al. Christensen, T. R. (2017). Exchange of co2 in arctic tundra: Impacts of

- 989 meteorological variations and biological disturbance. *Biogeosciences*, 14(19), 4467-4483.
 990 Retrieved from <https://bg.copernicus.org/articles/14/4467/2017/>. doi:10.5194/bg-14-
 991 4467-2017
- 992 Melton, J. R., Chan, E., Millard, K., Fortier, M., Winton, R. S., Martín-López, J. M., et
 993 al. Verchot, L. V. (2022). A map of global peatland extent created using machine learning
 994 (peat-ml). *Geosci. Model Dev. Discuss.*, 2022, 1-44. Retrieved from
 995 <https://gmd.copernicus.org/preprints/gmd-2021-426/>. doi:10.5194/gmd-2021-426
- 996 Qiu, C., Zhu, D., Ciais, P., Guenet, B., Peng, S., Krinner, G., et al. Hastie, A. (2019). Modelling
 997 northern peatland area and carbon dynamics since the holocene with the orchidee-peat
 998 land surface model (svn r5488). *Geosci. Model Dev.*, 12(7), 2961-2982. Retrieved from
 999 <https://gmd.copernicus.org/articles/12/2961/2019/>. doi:10.5194/gmd-12-2961-2019
- 1000 Vitt, D. H. (2013). Peatlands ☆. In B. Fath (Ed.), *Encyclopedia of ecology (second edition)* (pp.
 1001 557-566). Oxford: Elsevier.
- 1002 Xu, J., Morris, P. J., Liu, J., & Holden, J. (2018). Peatmap: Refining estimates of global peatland
 1003 distribution based on a meta-analysis. *CATENA*, 160, 134-140. Retrieved from
 1004 <https://www.sciencedirect.com/science/article/pii/S0341816217303004>.
 1005 doi:<https://doi.org/10.1016/j.catena.2017.09.010>